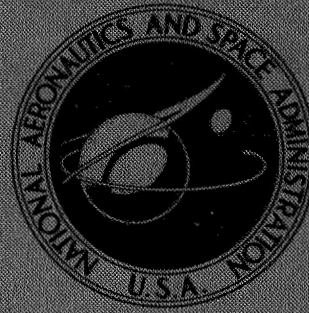


NASA TECHNICAL
MEMORANDUM



NASA TM X-1470

NASA TM X-1470

FACILITY FORM 602

N67-40224 (ACCESSION NUMBER)	
51 (PAGES)	1 (THRU)
/	31 (CODE)
(NASA CR OR TMX OR AD NUMBER)	(CATEGORY)

WIND-TUNNEL INVESTIGATION OF
SATURN S-IC AERODYNAMIC ENGINE GIMBAL
FORCES AND BASE PRESSURES USING A
COLD-FLOW-JET SIMULATION TECHNIQUE

by Bernard J. Blaha, Robert A. Wasko, and Donald L. Bresnahan

*Lewis Research Center
Cleveland, Ohio*

WIND-TUNNEL INVESTIGATION OF SATURN S-IC AERODYNAMIC ENGINE
GIMBAL FORCES AND BASE PRESSURES USING A
COLD-FLOW-JET SIMULATION TECHNIQUE

By Bernard J. Blaha, Robert A. Wasko, and Donald L. Bresnahan

Lewis Research Center
Cleveland, Ohio

NATIONAL AERONAUTICS AND SPACE ADMINISTRATION

For sale by the Clearinghouse for Federal Scientific and Technical Information
Springfield, Virginia 22151 - CFSTI price \$3.00

WIND-TUNNEL INVESTIGATION OF SATURN S-IC AERODYNAMIC ENGINE
GIMBAL FORCES AND BASE PRESSURES USING A
COLD-FLOW-JET SIMULATION TECHNIQUE

by Bernard J. Blaha, Robert A. Wasko, and Donald L. Bresnahan

Lewis Research Center

SUMMARY

An investigation was made of the aerodynamic hinge moments of two of the F-1 engine nozzles on a 0.01585 scale model of the **S-IC** boost stage of the Saturn V launch vehicle utilizing a cold-flow-jet simulation technique. High-pressure dried air at room temperature was used for nozzle flow. The investigation was made over a Mach number range of 0.56 to 3.5 for 0° , 5° , and 10° angles of attack; 0° , 1.5° , and 3° gimbals angles; 0° and 45° roll angles; and for three sizes of base flow deflectors. Model base pressures were also investigated. Jet-on and jet-off comparisons were made to determine jet effects on both nozzle hinge moment and base pressures.

Nozzle-hinge-moment coefficients were increased by the presence of base flow deflectors. In general, hinge moments were maximum for Mach numbers between 0.56 and 1.66 and decreased with increasing Mach number. Maximum hinge-moment coefficients were measured at the largest angle of attack and gimbals angle tested for both roll angles. Jet flow generally increased the magnitude of hinge moments over those at the jet-off condition. Base pressure was increased by the presence of base flow deflectors at all Mach numbers. At lower Mach numbers, base pressures were constant across the base and less than free-stream static pressure. At high Mach numbers, base pressures were greater than free-stream static pressure and decreased from the inner to the outer regions of the base. Jet-on base pressures were less than pressures at jet-off conditions below Mach 1.0 but greater at higher speeds.

INTRODUCTION

During launch, thrust vector control of the Saturn V boost vehicle is obtained by gimbaling the four outboard rocket engines. Airstream impingement on the nozzles

could generate large hinge moments which in turn could result in high actuator loads or reductions in the gimbal rates of the engines. Consequently, it is beneficial to determine the magnitudes of aerodynamic loads that exist on the nozzles at various flight conditions. References 1 and 2 present results of scale-model tests in which nozzle hinge moments were determined for various flight conditions and vehicle configurations. However, no internal nozzle flow was used to simulate jet effects. Interactions of jet plumes with each other and with the free stream produce large effects on the pressure field in the vehicle base region. This in turn may influence the aerodynamic nozzle loads.

In an attempt to determine hinge moments on the F-1 nozzles with jet flow, wind-tunnel tests were conducted at transonic and supersonic speeds on a 0.01585 scale model of the S-IC stage of the Saturn V launch vehicle utilizing a cold-flow-simulation technique. Internal nozzle geometry on the model was designed to produce jet pluming which conforms to the jet simulation parameters described in references 3 and 4. High-pressure dried air at room temperature was used to simulate the nozzle exhaust gases. Nozzle chamber pressure was varied from 300 psia ($2.07 \times 10^6 \text{ N/m}^2$) to 1100 psia ($7.58 \times 10^6 \text{ N/m}^2$) to simulate the exit-static-pressure to ambient-pressure ratio of the full-scale F-1 engine over the launch trajectory. Model tests were conducted in the Lewis 8- by 6-foot and the 10- by 10-foot supersonic wind tunnels at free-stream Mach numbers from 0.56 to 3.5. Nozzle-hinge-moment and base-pressure data were obtained for nozzle gimbal angles of 0° , 1.5° , and 3° ; model angles of attack of 0° , 5° , and 10° ; and model roll angles of 0° and 45° . Jet-on and jet-off comparisons were made for various combinations of the abovementioned parameters. Also, an investigation was made to determine the effect of three sizes of base flow deflectors on nozzle hinge moments and base pressures.

SYMBOLS

A	reference area of model nozzle at exit station, 4.09 in. ² (26.41 cm ²)
A _E	flow area at model nozzle exit, 3.24 in. ² (20.92 cm ²)
A*	area of nozzle throat, 0.621 in. ² (4.01 cm ²)
C _{H_N}	nozzle-hinge-moment coefficient in direction of normal force, $N/q_o Ad$
C _{H_Y}	nozzle-hinge-moment coefficient in direction of side force, $Y/q_o Ad$
	local static pressure coefficient, $(p_x - p_o)/q_o$
d	reference diameter of model nozzle exit (outside diameter), 2.282 in. (5.80 cm)
h	height of base flow deflectors

M_E	Mach number of jet at nozzle exit
M_O	free-stream Mach number
N	hinge-moment component in normal force plane
P_c	nozzle plenum chamber stagnation pressure
p_b	local baseplate static pressure
\bar{p}_b	average baseplate static pressure
p_E	average nozzle-wall-exit static pressure
p_O	free-stream static pressure
p_x	local static pressure on model nozzle external surface
q_O	free-stream dynamic pressure
R	radius of model base, 3.14 in. (7.96 cm)
r	radial distance of baseplate static pressure orifice measured from model centerline
$\dot{w}_{\text{deflectors}}$	weight flow through base flow deflectors
\dot{w}_{base}	weight flow through free-stream tube with an area equal to vehicle base area
x	longitudinal distance from model base to pressure orifice on nozzle
Y	hinge-moment component in side force or yaw plane
α	model angle of attack
β	nozzle gimbal angle {measured in model pitch plane}
γ_E	ratio of specific heats of exhaust gas at nozzle exit
φ	model roll angle
θ_E	internal exit angle or discharge angle of nozzle

APPARATUS AND PROCEDURE

External Model Geometry

Figure 1 shows a schematic drawing of the model installation in both the 10- by 10-foot and the 8- by 6-foot supersonic wind tunnels. The model was strut mounted from the ceiling in both tunnels; however, a different strut was used in each tunnel. A vertical strut was used in the 10- by 10-foot tunnel, whereas a swept strut was used in the

8- by 6-foot wind tunnel to provide a uniform distribution of blockage area so that the maximum local blockage did not exceed 1.4 percent. Instrumentation and high-pressure air were brought into the model through the struts. The model was 73.3 inches (186.0 cm) long and 6.28 inches (15.93 cm) in diameter. The upper stages of the Saturn V launch vehicle were not simulated on the model but were replaced by a cone cylinder forebody which enclosed a high-pressure plenum chamber common to the five exhaust nozzles. A 15° half-angle cone was used for the forebody nose. The models were tested over the complete Mach number range of each tunnel: Mach 0.56 to 2.0 in the 8 by 6 and Mach 2.0 to 3.5 in the 10 by 10.

A comparison of the external shape of the cold-flow nozzle to the full-scale engine geometry is shown in figure 2. The scaled nozzles were designed to provide the best practical simulation of the F-1 engine external contour. However, near the nozzle throat the geometry could not be simulated because of a difference in area ratio A/A^* (16 for the full scale and 5.22 for the model nozzle). This difference arises from the cold-flow-simulation technique utilized for the model nozzle design. The outside diameter of the F-1 full-scale engine nozzle at the exit was 144.0 inches (366.0 cm) and was the basis of the scale factor for the model components.

Static pressure instrumentation was installed on two of the model nozzles, as shown in figure 3. Eighty pressure orifices were arranged in eight rows of ten each over 360° of the nozzle external surface. By integration of these pressure forces, the moment coefficients in both the normal and yaw directions were calculated. The sign convention used to define the nozzle loads is shown in figure 4. Hinge-moment coefficients were referred to a nozzle body-axis system with the origin located at the gimbal center which, as shown in figures 3 and 4, was in the plane of the model baseplate. This axis system was held fixed throughout the testing so that it rotated with model roll angle, as shown in the schematic drawing of the model base at 45° roll angle.

The locations of the instrumented nozzles and the gimbal configurations tested are shown in figure 5. Instrumentation was installed on the outboard engines only. Gimbal angles of 0°, 1.5°, and 3° were investigated at roll angles of 0° and 45°. These gimbal angles were always in a direction that tended to decrease the vehicle angle of attack which covered a range from 0° to 10°. The center nozzle remained at 0° gimbal for each configuration. A change in gimbal configuration was accomplished by replacing the complete aft portion of the model including the nozzle plenum chamber. At 45° roll and 3° gimbal angles, data were also obtained on the lower nozzle (fig. 5(f)).

The model base at 45° roll and 0° gimbal angles is shown in figure 6. Included in the figure are the nozzles, nozzle shrouds, fins, and the largest flow deflectors. Details of the nozzle shroud and fin are presented schematically in figure 7. Details of three base flow deflectors that were tested are shown in figure 8.

Base flow deflectors are used on the prototype to introduce stream flow into the

base region for cooling. The first deflector configuration ($h = 0.317$ in. (0.805 cm)) was based on a simple geometric scaling of the prototype deflector height. Because of the model length and the differences from flight values of Reynolds numbers in the two tunnels, the model boundary layer at the deflector station was larger than flight over the Mach number range tested. Therefore, the geometric scale deflectors would not be expected to deflect the proper weight flow of stream air into the model base region. In an effort to correct for this, the other sizes of flow deflectors were tested. The large configuration ($h = 0.574$ in. (1.458 cm)) was based on a weight flow scaling parameter, resulting in a deflector height of 1.81 times the geometric scale height. This scaling parameter specifies that for each test condition

$$\frac{\dot{w}_{\text{deflectors}}}{\dot{w}_{\text{base}}} = \frac{\dot{w}_{\text{deflectors}}}{\dot{w}_{\text{base}}}$$

where $\dot{w}_{\text{deflectors}}$ is the weight flow through the deflectors and \dot{w}_{base} is the weight flow through a stream tube with an area equal to the base area. The height of the intermediate configuration ($h = 0.476$ in. (1.21 cm)) was arbitrarily chosen as 1.5 times the geometric scale height. All three sizes were based on the prototype circumferential gap of 11° between deflectors. Hereinafter, the deflectors are referred to as the geometric scale deflector, the 1.5 deflector, and the 1.81 deflector.

Details of baseplate instrumentation are shown in figure 9. Also shown are static pressure orifices located on the internal surfaces of the nozzle walls. Two orifices were installed on each nozzle as close to the exit as possible. These orifices were used to determine the average exit pressure of the nozzles. Since the orifice could not be positioned exactly at the exit station, one-dimensional flow corrections were made to yield the true wall exit pressure.

Internal Nozzle Geometry and Test Procedure

Internal nozzle geometry was designed to produce jet pluming which conforms to the jet-simulation parameters, as defined in references 3 and 4. Basis for the simulation arises from inviscid flow relations and predicts that, at high exit-pressure ratios, the initial plume shape immediately downstream of the nozzle can be simulated. The difference in the specific heat ratios γ_E of the cold air used in the model and the prototype hot exhaust gas is accounted for by adjusting the model area ratio A_E/A^* in accordance with the following relation:

$$\left(\frac{\gamma_E M_E^2}{\sqrt{M_E^2 - 1}} \right)_{\text{model}} = \left(\frac{\gamma_E M_E^2}{\sqrt{M_E^2 - 1}} \right)_{\text{prototype}}$$

Nozzle chamber pressure is then adjusted in accordance with the following relation:

$$\left[\frac{p_o}{P_c} \left(1 + \frac{\gamma_E - 1}{2} M_E^2 \right)^{\gamma_E/\gamma_E} \right]_{\text{model}} = \left[\frac{p_o}{P_c} \left(1 + \frac{\gamma_E - 1}{2} M_E^2 \right)^{\gamma_E/\gamma_E} \right]_{\text{prototype}}$$

which, in effect, results in the exit pressure ratio of the model equaling the full-scale ratio:

$$\left(\frac{p_E}{p_o} \right)_{\text{model}} = \left(\frac{p_E}{p_o} \right)_{\text{prototype}}$$

The simulation rules also require that the discharge angle of the model nozzles equal the prototype angle. For the **0.01585** scale model, it was impractical to scale the prototype nozzle wall thickness because the resulting wall thickness, **0.016 inch (0.041 cm)**, was considered too thin for structural integrity and the installation of the desired instrumentation. Consequently, the model nozzle-exit-wall thickness was **0.125 inch (0.317 cm)**. Since the outside diameter of the nozzle was geometrically scaled, the inner diameter was then smaller than the geometric scale value. Since gimbal loads were expected to be critical at transonic speeds, the model discharge angle was adjusted from **11°** (prototype) to **17°** thereby causing jet impingement to occur at the same pressure ratio (**2.3**) as would occur in flight at Mach **1.2**. This compromise in model design then results in excessive jet impingement at the higher Mach numbers. A comparison between the full-scale and resulting model nozzle design characteristics is summarized in table I. The values used for the **F-1** engines were the best estimate that existed at the time of the model tests.

Test procedure, therefore, was to adjust the nozzle chamber pressure between **300 psia (2.07x10⁶ N/m²)** and **1100 psia (7.58x10⁶ N/m²)** to yield a nozzle exit pressure so that the p_E/p_o ratio would equal the flight value at each test condition. The flight pressure ratios were calculated from the estimated prototype nozzle exit static pressure of **11 psia (7.58x10⁴ N/m²)** and the S-IC launch trajectory. Figure 10 shows a typical launch trajectory for the S-IC booster, and also the altitude trajectories of both the 8-

by 6- and 10- by 10-foot supersonic wind tunnels. The 10- by 10-foot tunnel conditions were adjusted to match flight trajectory; therefore, the chamber pressure was kept constant yielding an exit static pressure of 11 psia ($7.58 \times 10^4 \text{ N/m}^2$). The 8- by 6-foot tunnel trajectory was considerably below flight; consequently, the chamber pressure was adjusted at each Mach number to keep the exit pressure ratio equal to that of flight. The nozzle-exit-pressure-ratio schedule used for testing in the two tunnels is presented in figure 11. As seen in the figure, a discontinuity exists in the schedule near Mach 2.0. This discontinuity arose because, in the interim between tests in the two facilities, a revised estimate was made for the altitude trajectory of the launch vehicle which was slightly different near Mach 2.0. This revision did not significantly alter the altitude trajectory shown in figure 10 but did result in the discontinuity shown in figure 11. In the 8- by 6-foot tunnel testing, additional off-trajectory data were obtained to determine jet effects on both nozzle hinge moment and base pressure for a range of p_E/p_O .

RESULTS

Hinge-Moment Coefficients

Effects of base flow deflectors. - Hinge-moment coefficients are shown in figure 12 as a function of Mach number for the normal and side forces on the upper and lower nozzles (A and B, respectively) at 0° roll angle. Data are presented for three sizes of base flow deflectors. The data are for jet-on conditions with nozzle-exit-pressure ratio p_E/p_O set equal to the flight values shown in figure 11. Trends seen for the gimbal angles of 0° and 3° were essentially the same for the other test configurations. In general, the moment coefficients were large at transonic Mach numbers and decreased with increasing Mach number, being nearly zero at Mach 3.5. At 0° gimbal angle and 0° angle of attack (fig. 12(a)), the hinge-moment coefficients on both the upper and lower nozzles indicated that the nozzles experienced forces generally directed outboard from the center nozzle.

Within the range of variables investigated, the two larger base flow deflectors increased the magnitude of the moment coefficients in the normal force direction from those measured with the small deflectors. The greater mass flow deflected by the large deflectors increased the pressures on the inboard surfaces of the nozzles so that the normal forces were increased. However, as evidenced from the coefficients measured in the yaw direction, the effect was not symmetrical. Yaw coefficients on the upper nozzle decreased at 0° gimbal angle for the 1.5 deflectors and increased for the 1.81 deflectors. The asymmetries that were apparent may have been a result of support strut wake interference effects on the top nozzle (A). Differences in force coefficients were

also apparent between the two tunnels at the same Mach number (2.0). Factors contributing to these differences were changes in model boundary layer due to Reynolds number effects, differences in possible wall reflected disturbances originating from the support system, and differences in the nozzle exit pressure ratio p_E/p_0 .

At 3° gimbale angle (fig. 12(b)), a greater asymmetry of forces between the top and bottom nozzles became apparent since the gimbale directions were not symmetrical. The trend of the effect of flow deflector size on hinge moments in the normal force direction was the same as at 0° gimbale angle. However, those measured in the yaw direction showed almost no effect of deflector size. The moments were still highest at transonic speeds and decreased at the higher speeds. Also, the moments indicated that the forces for 3° gimbale angle were still outboard, except on the lower nozzle (B) at Mach numbers greater than 2.5 when the moments in the normal direction became inboard.

Similar data for a model roll angle of 45° are presented in figure 13 for 0° gimbale angle and 0° angle of attack. Results for the 1.5 deflectors were almost identical to the 1.81 deflectors; consequently, they are not presented. With this configuration, data without flow deflectors were obtained for Mach numbers between 0.56 and 1.37. The trends at 45° roll angle were generally the same as those at 0° but variations in the asymmetries again suggested strut wake interference effects and wall reflected disturbances on the top nozzle (A). The moments were again highest at transonic speeds and outboard in direction, and the deflectors generally increased the moment coefficients in such a manner as to increase the outboard directed forces.

Some of the trends seen at both 45° and 0° roll angles can be explained with the aid of the nozzle static pressure distributions presented in figure 14. Local static pressure coefficient C_P on nozzle B is plotted as a function of the dimensionless position coordinate x/d for two longitudinal rows of pressure orifices on the nozzle external surface: one inboard (close to center of model base) and one outboard (close to the nozzle shroud). Data are presented at 0° gimbale angle and 0° angle of attack for a range of nozzle-exit-pressure ratio (or Mach number) and are representative of results seen on the other nozzles. In general, the nozzle pressures were less than free-stream static pressure at low pressure ratio (fig. 14(a)) and were greater at high pressure ratio (fig. 14(d)). The pressures on the nozzle were low near the base where the magnitudes were close to the local base pressure and were higher at larger x/d stations. The pressures on the inboard surface were always higher than or equal to those on the outboard surface. This accounts for the outboard directed forces measured on the nozzle and indicates that the resultant force on the nozzle was not related to the base pressure level as might be intuitively expected.

The magnitude of the pressure gradient across the nozzle, that is, the pressure differential from the inboard to the outboard surface, and the distance of the center of pressure on the nozzle from the gimbale center determine the magnitude of the hinge mo-

ment on the nozzle. The center of pressure on the nozzle was usually close to the position of the maximum pressure gradient which, as seen in figure 14, generally existed between $x/d = 0.8$ and **1.3**. The pressure gradients were large at the lower pressure ratios (or Mach numbers) and lower at the higher pressure ratios, which explains the trends seen in figures 12 and 13 where the hinge moments were maximum between Mach 0.56 and 1.66 and decreased at higher Mach numbers.

The effects of base flow deflectors were to increase the pressure level over the whole nozzle, to increase the magnitude of the pressure gradient across the nozzle, and to shift the station of maximum pressure gradient and center of pressure to larger values of x/d . The large deflectors had the largest effect. The latter two results account for the increase in hinge moment seen in figures 12 and 13 with an increase in deflector size. The shape of the pressure distributions on the nozzle with deflectors present indicates that perhaps the deflectors caused stream flow to impinge on the nozzle inboard surface at the larger x/d stations thereby producing the effects mentioned previously.

Because the large deflector data would be expected to result in the most conservative design of the flight vehicle, the large deflectors were used for most of model test conditions. Consequently, the following data presented in this report predominantly concern configurations utilizing these deflectors.

Effect of angle of attack and gimbal angle. - As shown in figure 15, the largest effects of angle of attack at 0° roll angle occurred on the upper nozzle (A) which was on the lee side of the model. In the normal force direction, the hinge-moment coefficients increased as model angle increased from 0° to 10° . As model angle increases, the lower outboard surface of the upper nozzle is rotated toward the windward side of the model; consequently, increased flow impingement results because of the upwash flow around the model body. Coefficients in the yaw direction generally decreased as angle of attack increased. For some test conditions, the sign of the coefficient changed indicating that the impingement of the upwash flow was significant enough to change the direction of the yaw force on the nozzle. At 10° angle of attack, this effect on the yaw forces was reversed for Mach numbers larger than **2.25** where the coefficients became positive and eventually exceeded those at 0° .

Similar effects were seen on the lower nozzle (B) with increasing angle. Since this nozzle was on the windward side of the model at angle of attack, the coefficients in the normal direction generally decreased in magnitude with increasing angle. Coefficients in the yaw direction generally increased with an increase in angle of attack. The magnitudes of the effects of angle of attack seen on the lower nozzle were not as large as on the upper nozzle. A probable reason is that, although the nozzle is on the windward side of the model at angle of attack, the shroud shields the lower nozzle from free-stream flow effects. At angle of attack, the position of the shroud on the upper nozzle causes it to be a less effective shield from the body upwash flow.

Comparison of figures 15(a), (b), and (c) shows that gimbale angle effects on nozzle hinge moment at 0° roll angle were essentially the same for each angle of attack. The most significant effect was seen in the normal direction on the upper nozzle (A) where the maximum moment coefficients at each angle of attack were increased with increasing gimbale angle. This again is the result of increased airstream impingement because positive gimbale at angle of attack results in a greater inclination of this nozzle toward the windward side of the model and the body upwash field.

The effect of angle of attack on nozzle hinge moment at 45° roll angle is shown in figure 16. The moment coefficients on the upper nozzle (A) were less sensitive to increases in angle of attack than those at 0° roll angle (fig. 15(a)) probably because, at 45° roll angle, the upper nozzle was well shielded at angle of attack by the model base. Coefficients measured on the lower nozzle (B) were more sensitive to model angle of attack. In this roll position, increased impingement from the body upwash field results, and the position of its shroud makes shielding the nozzle from the upwash flow less effective. At 10° angle of attack where the coefficients in the normal direction changed sign from negative to positive values, the effect of this upwash flow was especially evident. Also, the coefficients in the yaw direction increased with angle. In effect, the resultant force on the nozzle changed with model angle from an outboard to an upward direction.

These results are also evident in the nozzle static pressure distributions measured on nozzle B. Pressure coefficients are presented in figure 17 as a function of x/d for two longitudinal rows of orifices on the nozzle external surface: one on the bottom and one on the top. Data are presented at 45° roll and 0° gimbale angles with the 1.81 flow deflectors for jet-on conditions. At angle of attack, the data indicate that airstream impingement occurred on the lower surface of the nozzle between $x/d = 0.8$ and 1.0. This impingement resulted in increased pressures on the lower surface and consequently an increased pressure gradient across the nozzle from the lower to the upper surface. In turn, this increased pressure produced the results seen in figure 16 where the direction of the resultant force on nozzle B shifted with increased angle of attack from an outboard to an upward direction.

The effect of nozzle gimbale angle at 45° roll angle can be seen in figure 16. On the upper nozzle, the coefficients in both the normal and yaw directions increased as gimbale angle increased from 0° to 3° . The largest increases occurred between Mach 1.0 and 2.0. On the lower nozzle, an increase in gimbale angle magnified the effect seen with an increase in angle of attack. With both angle of attack and gimbale angle, increased airstream impingement occurs producing larger upward directed resultant forces on the nozzle than with angle of attack alone. Coefficients in the yaw direction on the lower nozzle also increased with gimbale angle.

Bottom engine at 45° roll angle. - Hinge moments measured on the bottom engine (C) at 45° roll and 3° gimbale angles are shown in figure 18. Data from the upper nozzle

(A) are also presented. Comparison of the two sets of data indicates that the bottom nozzle experienced smaller aerodynamic loadings than the upper nozzle and that the bottom nozzle forces were generally insensitive to model angle of attack. A comparison of these data with those in figure 16 (c) indicates that the side nozzle (B) experienced larger forces which were more sensitive to angle-of-attack effects than either the top or bottom nozzles.

Jet-on and jet-off conditions. - Comparisons of nozzle-hinge-moment coefficients for jet-on and jet-off conditions at 0° roll angle are made in figure 19. The results shown are for the three gimballed attitudes tested at 0° angle of attack. However, trends seen with these configurations were similar for all the configurations investigated. In general, jet flow increased the magnitude of hinge-moment coefficients measured in the normal force direction on both the upper and lower nozzles except at Mach 1.0. Increases on the upper nozzle with jet-on condition of up to 125 percent were measured for various test conditions and model configurations, for example, figure 19(c) at Mach 1.35. Coefficients measured in the yaw direction on the two instrumented nozzles showed both increases and decreases from the jet-off condition which varied with Mach number, configuration, and test variable. Some of these trends also can be seen in the nozzle-static-pressure distributions in figure 20. Nozzle pressures on nozzle B at 45° roll angle, 0° gimballed angle, and 0° angle of attack are presented as a function of x/d . These data are also representative of 0° roll angle.

At low nozzle-exit-pressure ratio (or Mach number), the static pressures on the nozzle decreased with jet-on condition, and at high exit-pressure ratio the static pressures increased with jet on. This is the result of jet-flow aspiration of the base region at low exit-pressure ratios, where the jets do not impinge, and pressurization of the base region at higher exit-pressure ratios, where the jets do impinge.

Although the pressure level significantly changed on the nozzle with jet on, the pressure distributions were only slightly altered. However, the pressure gradient from the inboard to the outboard surface of the nozzle showed an increase over the jet-off condition for pressures near the end of the nozzle (x/d greater than 1.0). This accounts for the increases in hinge-moment coefficient that were measured, for example, in figure 19. The results seen between the jet-on and jet-off conditions indicate that jet-off testing could yield hinge-moment coefficients that are lower in magnitude than those that might be seen in flight.

Variation with nozzle-pressure ratio. - In figure 21, hinge-moment coefficients are shown as a function of nozzle-exit- to ambient-static-pressure ratio. Data for the normal and yaw components on the lower nozzle (B) are presented at 45° roll angle, 0° gimballed angle, and 0° angle of attack. Results seen here were typical for both nozzles and for the range of model and nozzle attitudes investigated.

Data with and without the 1.81 deflector configurations are presented to span the

complete pressure ratio and Mach number ranges investigated: the no-deflector configuration was tested primarily at transonic Mach numbers (lower pressure ratios), while the deflector configurations were tested primarily at supersonic Mach numbers (higher pressure ratios). As seen previously in figures 12 and 13, the flow deflectors increased the magnitudes of the hinge moments. This was also true for the data presented in figure 21, but here the deflector data were presented to demonstrate the trends that exist at the higher pressure ratios. It is assumed that these same trends would exist for the no-deflector case at the higher pressure ratios.

Data from 0.01585 scale-model tests of an early S-IC configuration conducted in the same facilities are also presented to supplement the data from the present model tests. This configuration included a set of flow deflectors installed in the nozzle shrouds (known at the time as scoops) and a set of base flow deflectors that correspond to the present 1.5 flow deflectors. Subsequent to the testing of this configuration, a redesign of the prototype resulted in the removal of the scoops from the shrouds and a reduction in the size of the full-scale base flow deflectors.

At the lower pressure ratios (or Mach numbers) the hinge-moment coefficients in the normal force direction (fig. 21(a)) varied both with pressure ratio and free-stream Mach number. At these low pressure ratios, the jet plumes do not impinge; consequently, the base pressure field and resulting nozzle loads are influenced by both jet-flow effects and free-stream effects. For a given value of nozzle-exit-pressure ratio, the resulting nozzle loads vary with Mach number. For a given Mach number, the loads varied with pressure ratio; however, the nature of this variation was different at each Mach number. At the higher pressure ratios, the hinge-moment coefficients seemed to be less influenced by free-stream effects and more a function of nozzle-pressure ratio. At these pressure ratios, the jets were impinged causing the local pressure field to be strongly influenced by jet-exhaust recirculation. As described in reference 5, strong jet-exhaust-recirculation effects tend to reduce free-stream effects. Therefore, it is probable that at these higher pressure ratios, the nozzle hinge moments were less a function of free-stream Mach number and more a function of nozzle-exit-pressure ratio, as implied by the dashed curve in figure 21.

Similar trends existed with the side forces on the nozzle as shown in figure 21(b). At low pressure ratios, the moment coefficients are dependent on both pressure ratio and Mach number; however, the data between Mach 0.7 and 1.37 for the no-deflector configuration do not show the large Mach number variation seen for the normal forces. At higher pressure ratios, the data again imply that the hinge moments were less dependent on free-stream effects.

Base Pressures

Jet-on and jet-off comparison for average base pressure. - The average base pressure (a numerical average of pressure orifices in fig. 9) as a function of Mach number is presented in figure 22 for jet-on and jet-off conditions. Data for the no-deflector and 1.81-deflector configurations are presented at 45° roll angle, 0° gimbal angle, and 0° angle of attack. References 3 to 6 present detailed discussions of jet flow in the base of rocket-powered vehicles. The trends seen in figure 22 for the 0.01585-scale cold-flow model agree favorably with the results discussed in these references.

Jet-off base pressures decrease with increasing Mach number. This effect is normally observed for axisymmetric bodies with blunt bases. For Mach numbers up to 1.0, jet-on base pressures also decreased with Mach number; however, they were lower than jet-off values. This occurred because, in this Mach range, the jets are overexpanded and do not impinge; consequently, the jets act as ejector pumps and reduce the pressure in the base. As free-stream Mach number increases (concurrent with an increase in altitude), the jets expand and begin to interact with each other and the free stream, thereby producing stronger recirculation into the base. Eventually, the jets become fully impinging and the base becomes pressurized ($\bar{p}_b/p_o > 1$).

The model nozzles were designed so that impingement should begin at Mach 1.2; consequently, the pressures above Mach 1.0 (fig. 22) increased with Mach number diverging from the jet-off values. Base pressurization occurred at approximately $M_o = 1.55$ with the large flow deflectors. Once base pressurization occurs, the local pressure field becomes primarily a function of jet effects rather than free-stream conditions. The effect of base flow deflectors was to increase the average base pressure at all Mach numbers for both jet-on and jet-off conditions. The largest increase in base pressure with jet-on occurred at Mach 1.0.

Effect of nozzle-pressure ratio. - Average base pressure ratio as a function of nozzle-exit- to ambient-pressure ratio p_E/p_o is shown in figure 23. In a manner similar to figure 21, data are presented with and without the 1.81-flow-deflector configurations to yield a complete range of p_E/p_o . Also, in a manner similar to figure 21, data from 0.01585 scale-model tests of an early **S-IC** configuration are presented to supplement the data from the present model tests.

The scaled nozzles were designed to produce jet-flow impingement at Mach 1.2 corresponding to a nozzle-exit-pressure ratio of 2.3. References 3, 4, and 6 predict that, for a four-nozzle-cluster configuration, if the jets impinge, the base pressure will be primarily a function of nozzle-exit-pressure ratio. Below impingement, free-stream effects influence the base and it is difficult to predict what the base pressure should be. Similar results were seen on the five-nozzle-cluster 0.01585 scale model. At the higher exit-pressure ratios, the data tended to fall on a line of constant slope indicating that

free-stream effects were small. At lower exit-pressure ratios, the data varied with both pressure ratio and Mach number. Also the slope of each curve varied as the Mach number changed.

Data from a 0.0222 scale hot-flow model of the Saturn S-IC tested in the same facilities (ref. 5) are also presented. The hot-flow model was 74.7 inches (185.5 cm) longer than the cold-flow model and consequently was positioned differently in the tunnel test section. At the higher exit-pressure ratios, the hot-flow-model data differ slightly from the cold-flow data. Because a consistent trend was not apparent, the deviation of these data from those of the cold-flow data is probably the result of scatter. At the lower exit-pressure ratios, the hot-flow base pressures were generally higher at corresponding Mach numbers probably, as explained in reference 5, because of a tunnel-flow phenomenon. The extreme length of the hot-flow model dictated locating the afterbody near the end of the perforated test section, a region of local flow acceleration at less than Mach 1.0. The cold-flow model was located so that its afterbody was not in this accelerated flow field. However, the ti-ends seen on the hot- and cold-flow models were similar with increasing Mach number and pressure ratio; therefore, it was concluded that a reasonable simulation of the prototype and hot-flow-model base flow fields was produced on the cold-flow model.

Base pressure distributions. - Base pressure distributions are presented in figure 24 at 45° roll angle for three base-flow-deflector configurations. Base- to ambient-pressure ratios for jet-on conditions are presented as a function of the dimensionless position coordinate r/R at 0° angle of attack and 0° gimbale angle. In general, the pressures were uniform at low Mach numbers and decreased from the inner to the outer regions of the base at higher Mach numbers. The effect of base flow deflectors was to increase the base pressure: the largest deflectors have the largest effect. The small difference in pressure level seen at Mach 2.0 between the 8- by 6-foot and 10- by 10-foot wind tunnels was the result of the slightly different p_E/p_O trajectories used in the two facilities.

SUMMARY OF RESULTS

An investigation was made of the aerodynamic hinge moments of two of the F-1 engine nozzles on a 0.01585 scale model of the s-IC boost stage of the Saturn V launch vehicle utilizing a cold-flow-jet simulation technique. High-pressure dried air at room temperature was used for nozzle flow. The investigation was made over a Mach number range of 0.56 to 3.5 for 0° , 5° , and 10° angles of attack; 0° , 1.5° , and 3° gimbale angles; 0° and 45° roll angles; and for three sizes of base flow deflectors. Model base pressures were also investigated. Jet-on and jet-off comparisons were made to deter-

mine jet effects on nozzle hinge moment as well as base pressure. The following results were obtained for the nozzle-hinge-moment coefficients:

1. In general, nozzle hinge moments were directed outboard and were greatest at transonic Mach numbers and decreased to near zero at Mach 3.5. At angle of attack, the largest hinge moments occurred with vehicle roll angle such that the nozzle was in the vehicle yaw plane. Because of increased flow impingement resulting from body upwash flow, the maximum hinge moments were measured at the largest angle of attack and gimbal angle tested.

2. Within the range of variables investigated, the predominant effect of base flow deflectors was to increase the nozzle-hinge-moment coefficients. The largest increases were seen with the largest deflectors.

3. Jet flow generally increased the hinge-moment coefficients in the normal force direction over those measured under jet-off conditions. Increases up to 125 percent were measured for various configurations and Mach numbers. The coefficients in the yaw direction both increased and decreased with jet-on condition dependent on Mach number, configuration, and test variable.

4. At low nozzle-exit- to ambient-pressure ratios, the hinge moments in the normal force direction varied both with pressure ratio and free-stream Mach number. Hinge moments in the side force direction showed similar trends except between Mach 0.7 and 1.37, where the moments were less sensitive to Mach number changes. At the high nozzle-exit-pressure ratios, the hinge moments in both the normal and side force directions were primarily a function of nozzle-exit-pressure ratio.

The following results were obtained for the model base pressures:

5. Below Mach 1.6, the average base pressure with the largest flow deflectors was less than the free-stream ambient pressure, but greater at higher Mach numbers. For all configurations, jet-on base pressure was less than jet-off pressure below Mach 1.0 but greater at higher Mach numbers, indicating that below Mach 1.0 the jets aspirated the base.

6. For the lower nozzle-exit- to ambient-static-pressure ratios where mutual jet impingement did not occur, the base pressure was a function of both nozzle-exit-pressure ratio and free-stream Mach number. For the higher nozzle-exit-pressure ratios, base pressure was primarily a function of nozzle-exit-pressure ratio.

7. Base flow deflectors generally increased the base pressures. The largest increase, for jet-on conditions, was measured with the largest deflectors at Mach 1.0.

8. Base pressures were essentially constant over the base at low Mach numbers but showed a decrease from the inner to the outer regions at high Mach numbers.

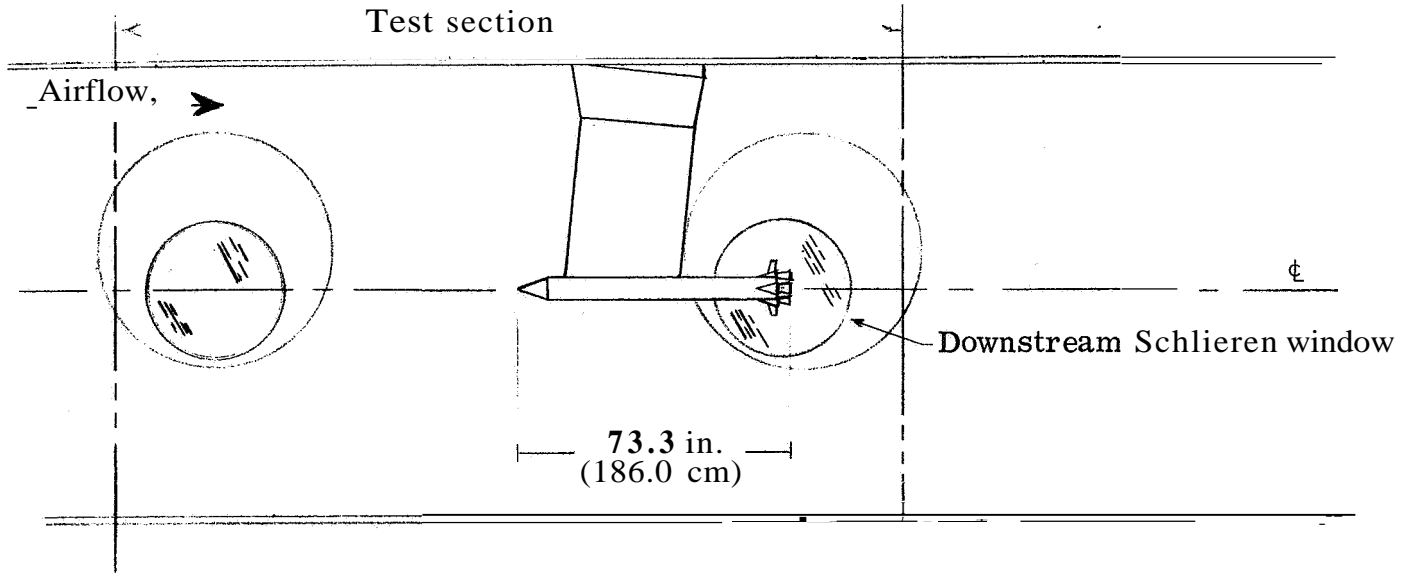
9. Base pressure on the cold-flow model of the Saturn S-IC showed favorable agreement with the base pressure on a hot-flow model tested in the same facilities.

Lewis Research Center,
National Aeronautics and Space Administration,
Cleveland, Ohio, October 3, 1967,
128-31-11-03-22.

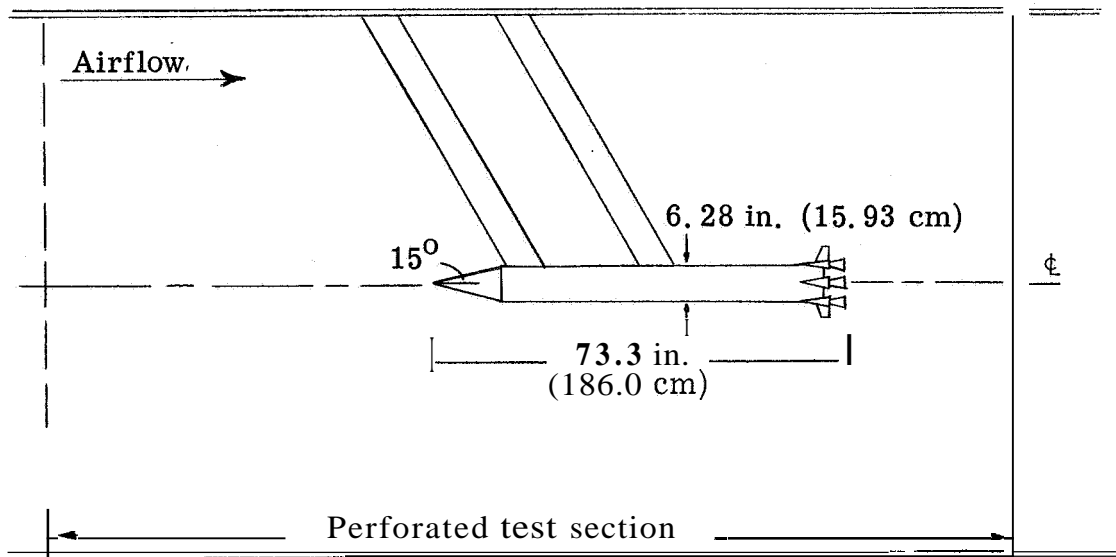
REFERENCES

1. Fuller, Dennis, E. ; and Charczenko, Nikolai: Wind-Tunnel Investigation of Nozzle Hinge Moments on Two Launch-Vehicle Models at Mach Numbers 1.60, 2.00, and 2.40. NASA TM X-954, 1964.
2. Ferris, James C. ; and Luoma, Arvo A. : Transonic Aerodynamic Nozzle Hinge Moments of F-1 Engine Without Internal Flow on a Model of the S-IC Stage of Saturn V. NASA TM X-1102, 1965.
3. Goethert, B. H. ; and Barnes, L. T. : Some Studies of the Flow Pattern at the Base of Missiles with Rocket Exhaust Jets. Rep. No. AEDC-TR-58-12, Arnold Engineering Development Center, June 1960.
4. Goethert, B. H. : Base Flow Characteristics of Missiles With Cluster-Rocket Exhausts. Aerospace Eng., vol. 20, no. 3, Mar. 1961, pp. 28-29, 108-117.
5. Wasko, Robert A. : Wind-Tunnel Investigation of Thermal and Pressure Environments in the Base of the Saturn S-IC Booster From Mach 0.1 to 3.5. NASA TN D-3612, 1966.
6. Wasko, R. A. ; and Cover, T. L. : Experimental Investigation of Base Flow Field at High Altitudes for Configurations of Four and Five Clustered Nozzles. NASA TM X-1371, 1967.

Engine characteristic	Prototype	Model
Nozzle area ratio, A_E/A^*	16	5.22
Ratio of specific heats for exhaust gas at nozzle exit, γ_E	1.22	1.4
Exit Mach number, M_E	3.65	3.22
Internal exit angle, θ_E , deg	11	17



(a) 10-by 10-foot tunnel.



(b) 8-by 6-foot tunnel.

Figure 1. - Schematic drawing of model installation in wind tunnels.

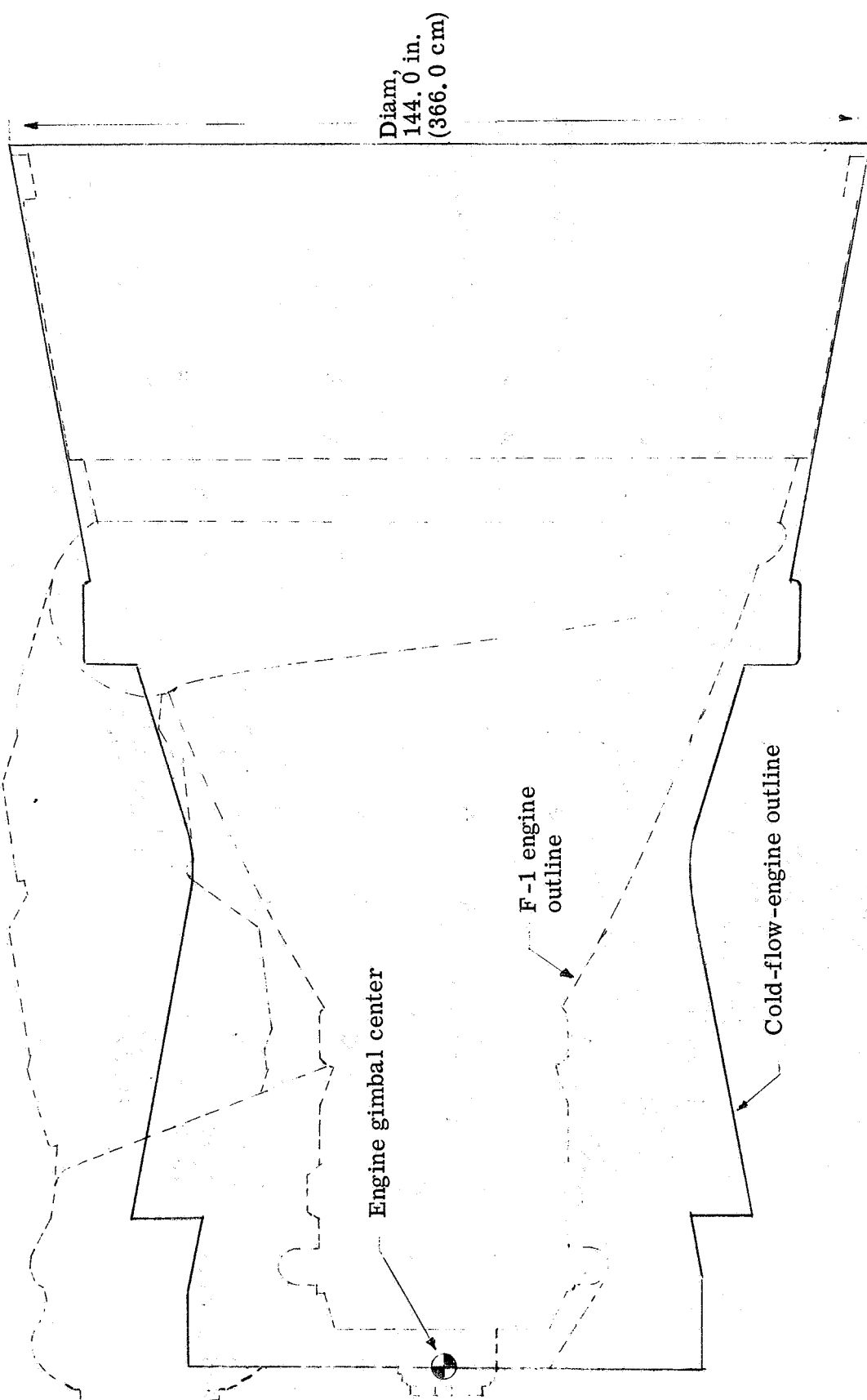


Figure 2. - Comparison of cold-flow-model and full-scale-engine geometries.

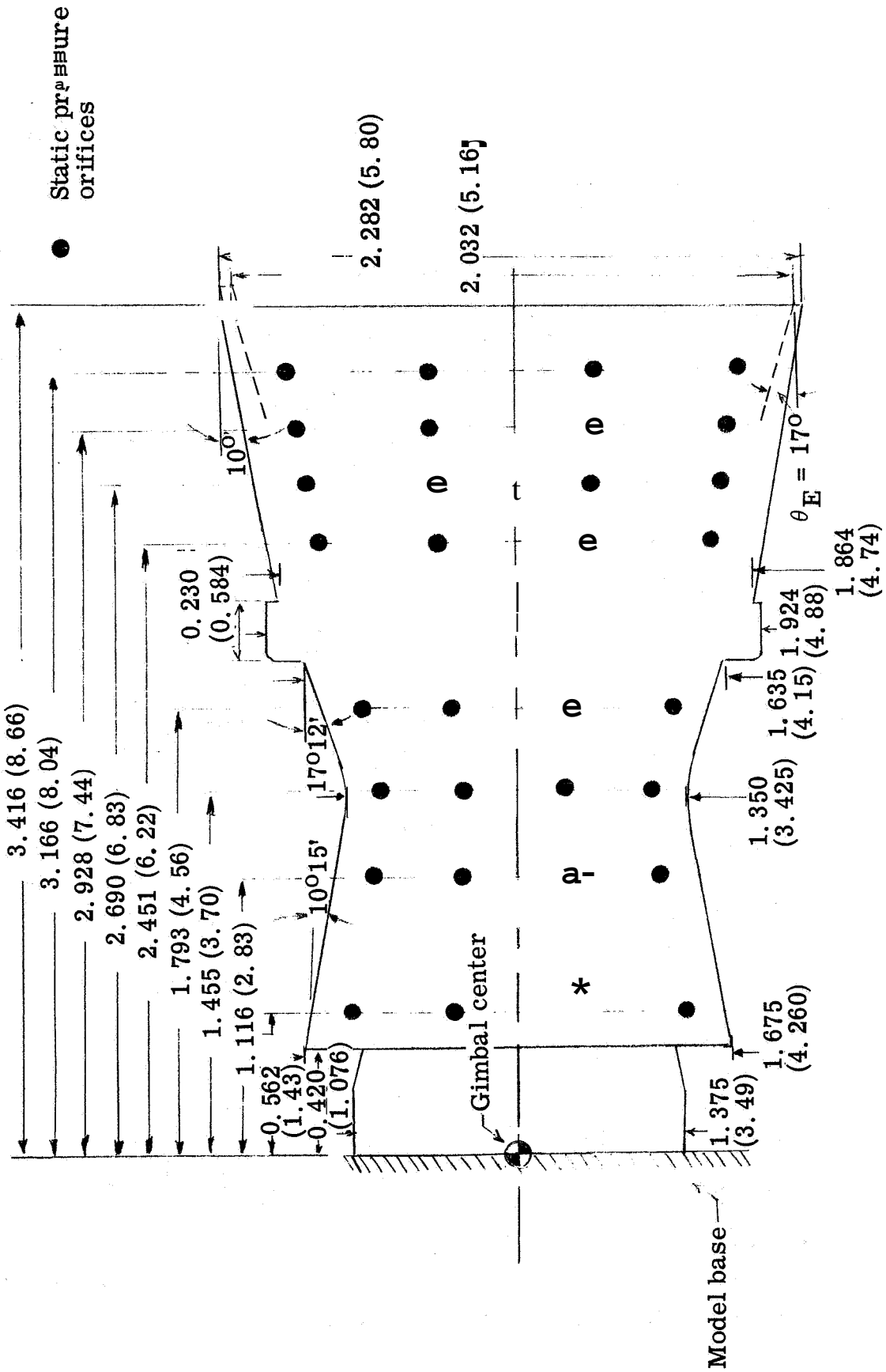


Figure 3. - Nozzle geometry and instrumentation details. (All dimensions are in inches (cm) unless otherwise noted.)

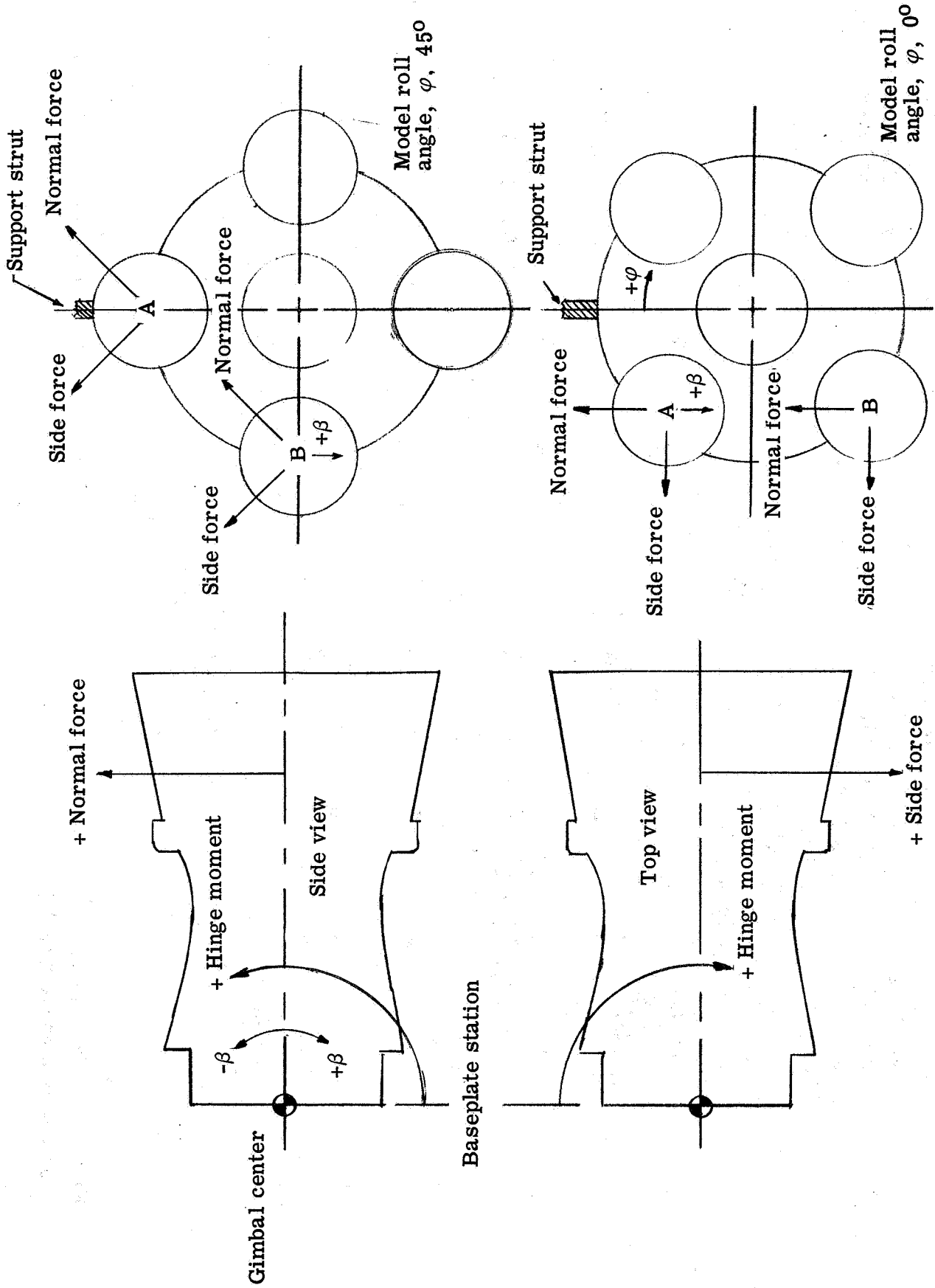


Figure 4. - Nozzle sign convention. Upper nozzle denoted by A; lower nozzle denoted by B.

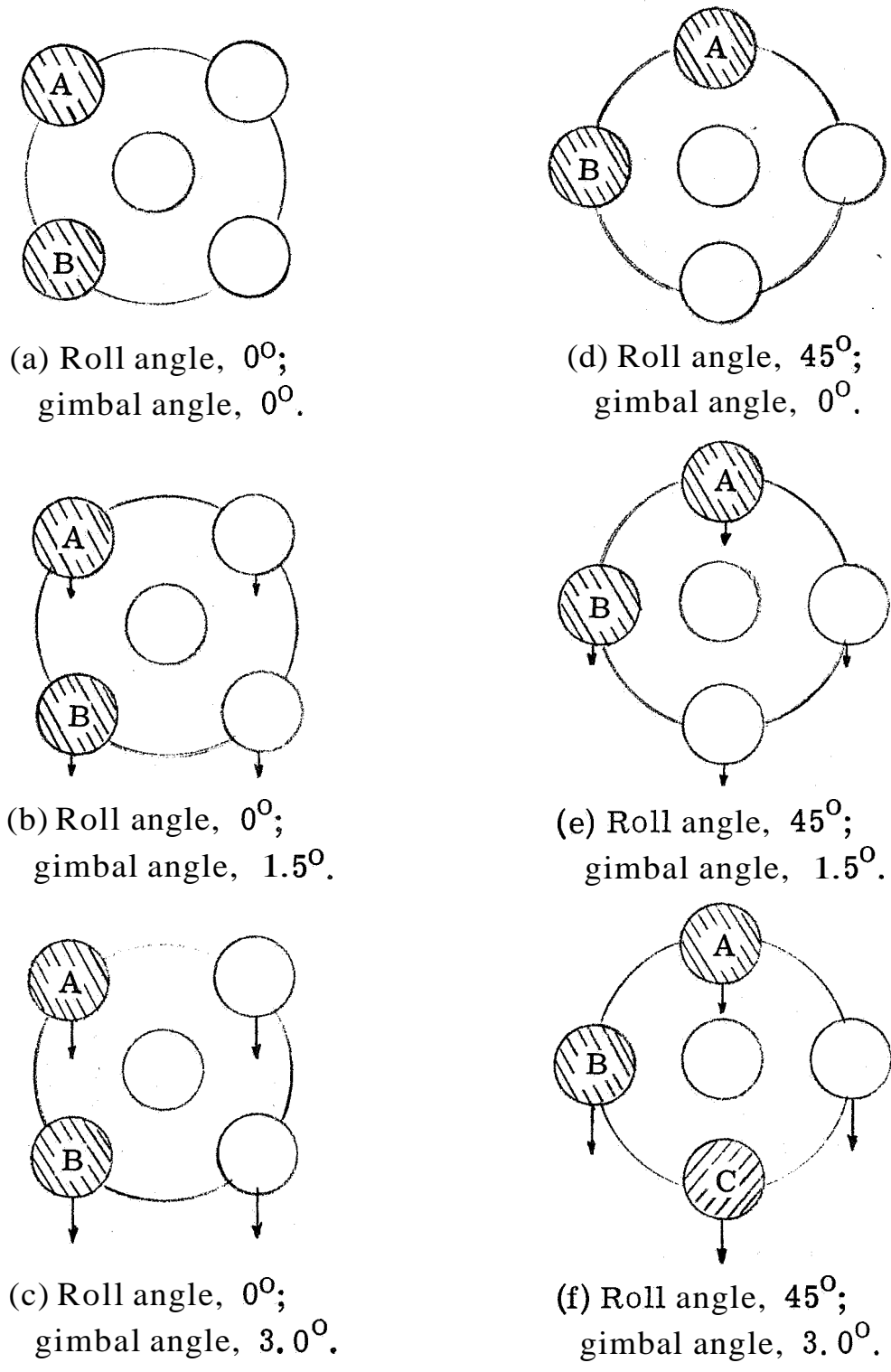


Figure 5. - Location of instrumented nozzles and description of nozzle gimbal patterns.

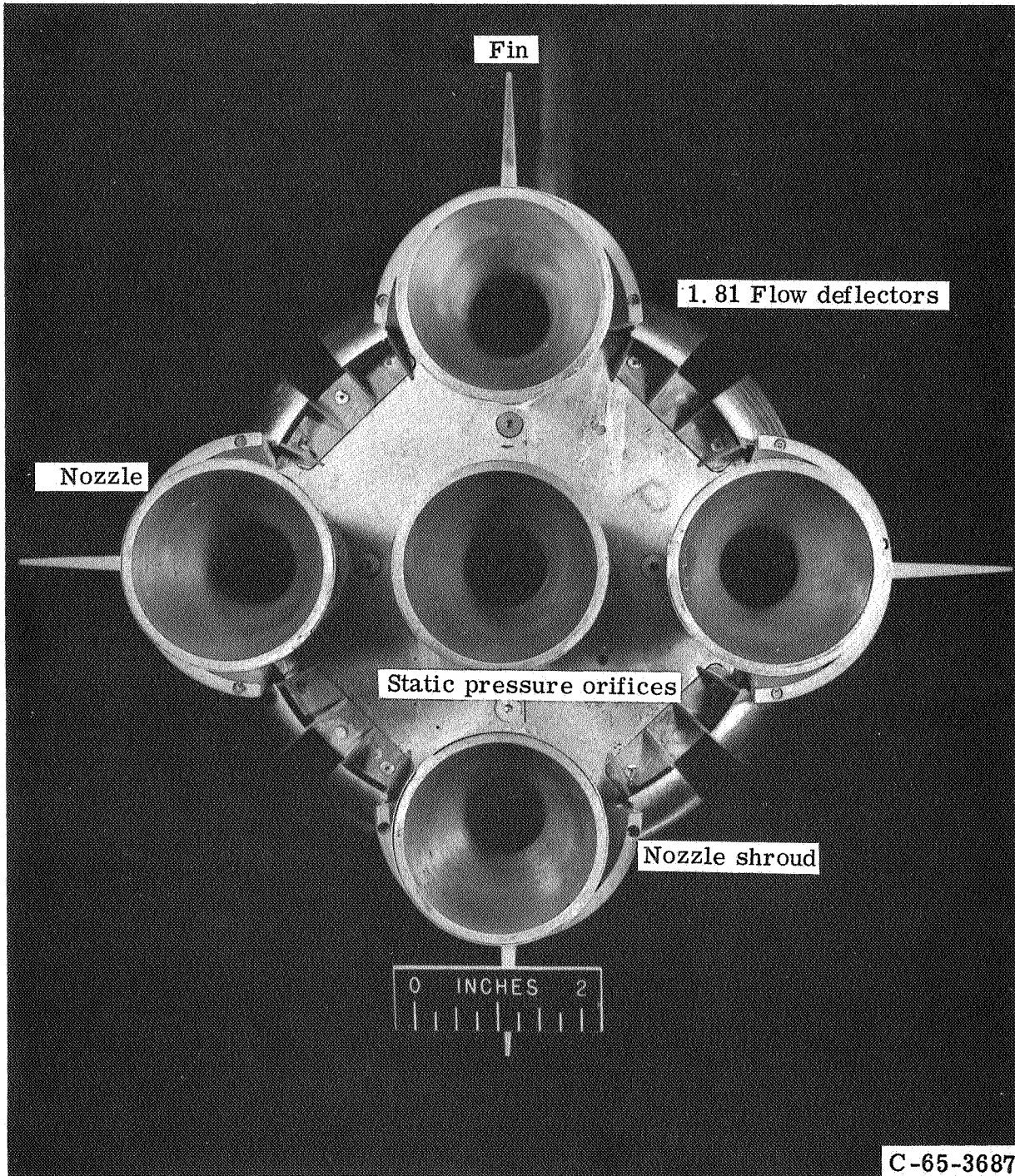


Figure 6. - Saturn S-IC 0.01585 scale-model base.

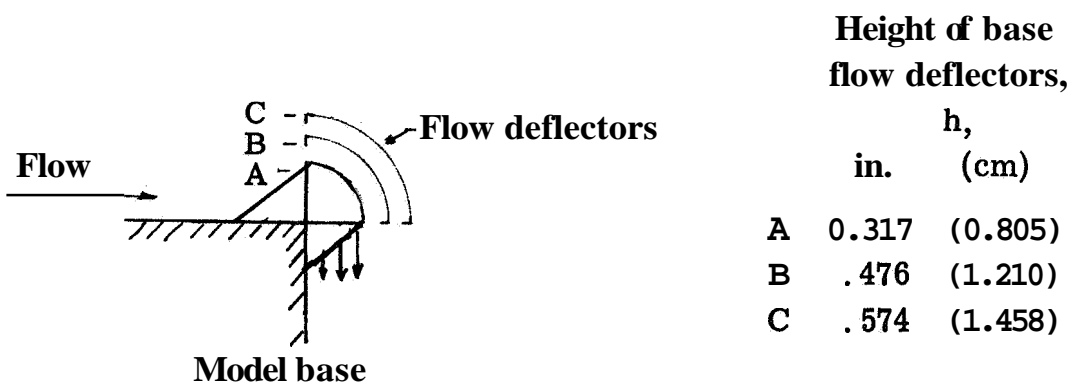
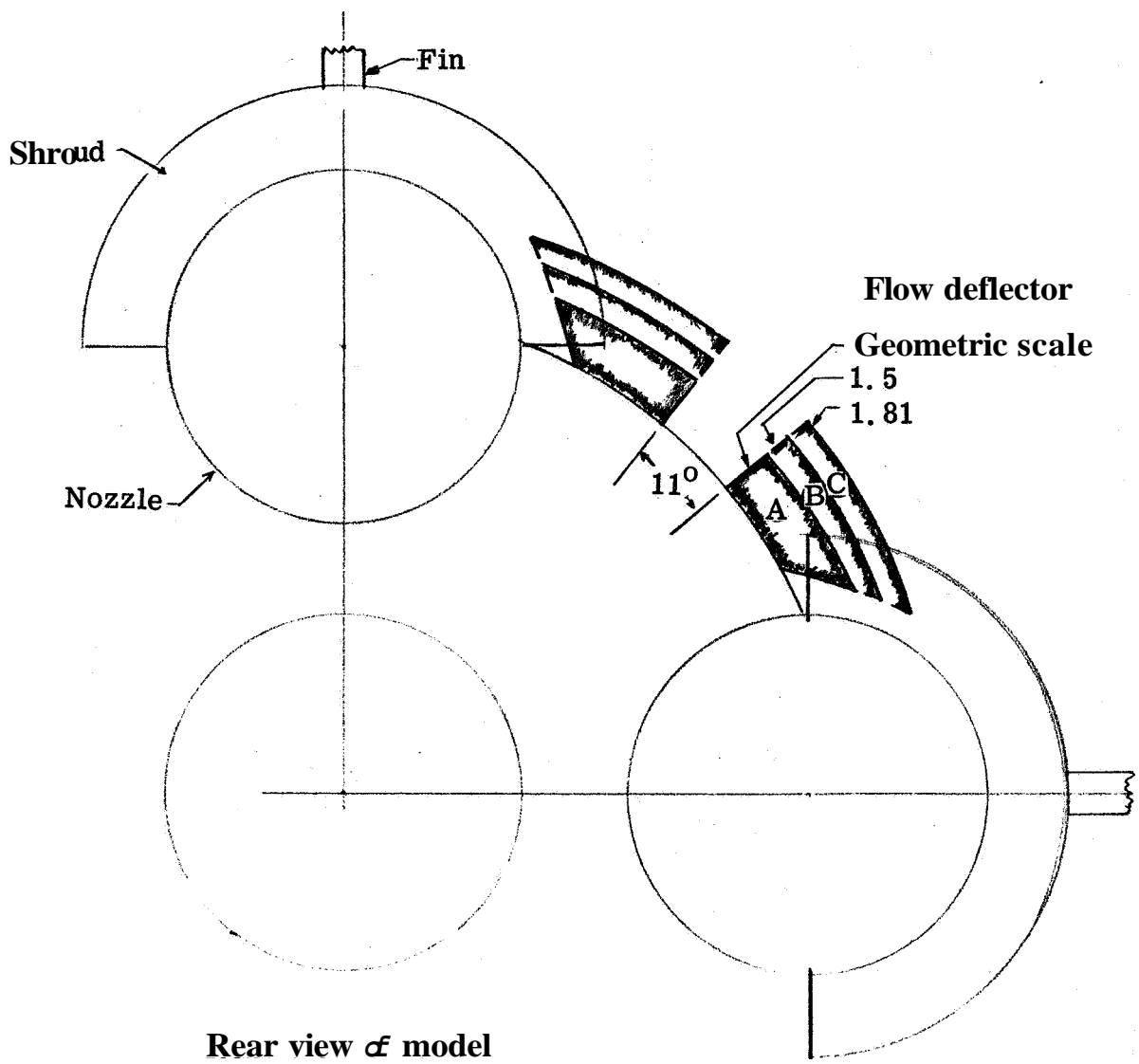


Figure 8. - Details of base flow deflectors.

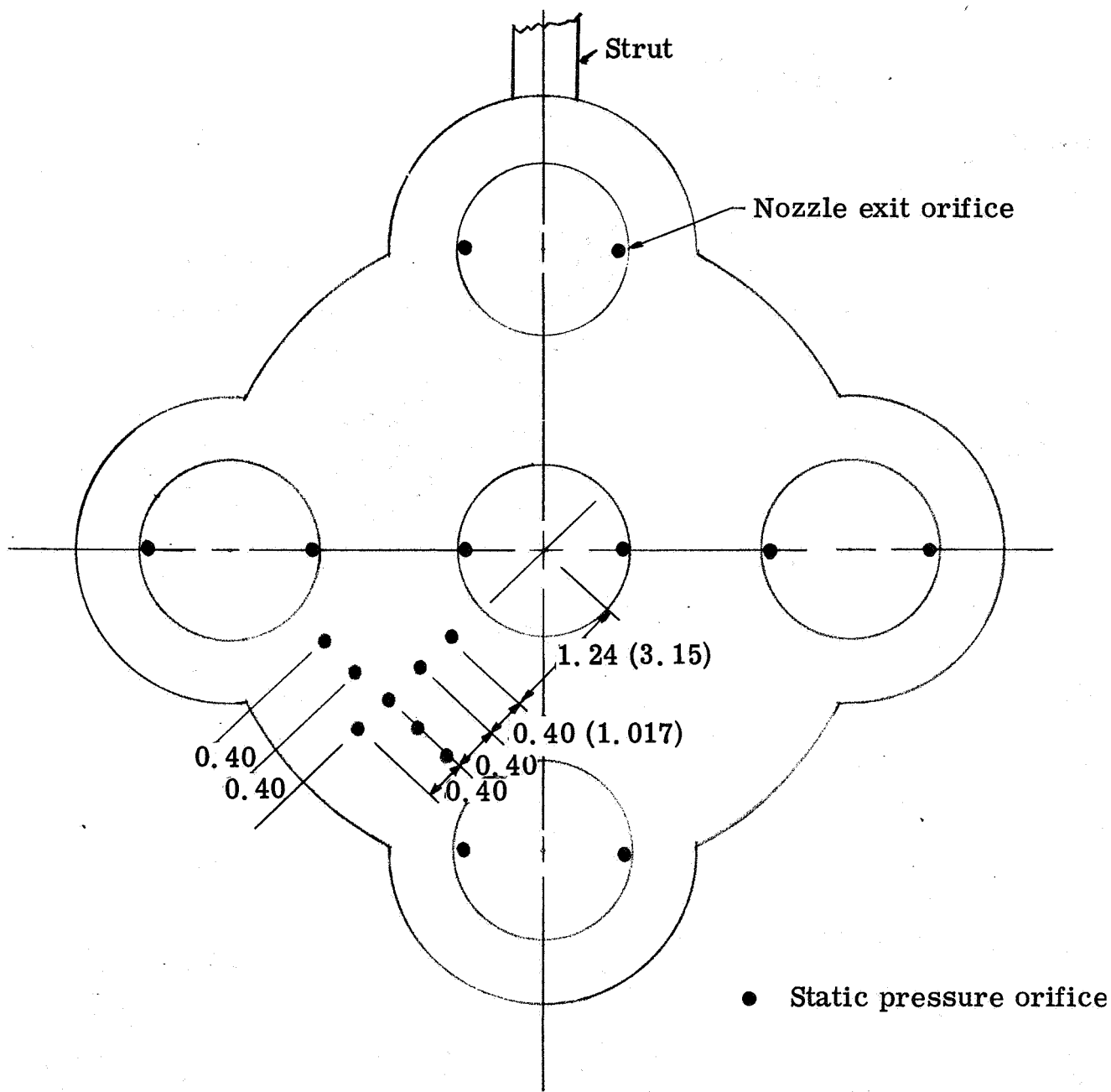


Figure 9. - Details of baseplate and nozzle-exit-pressure instrumentation.
 Model roll angle, 45° . (All dimensions are in inches (cm).)

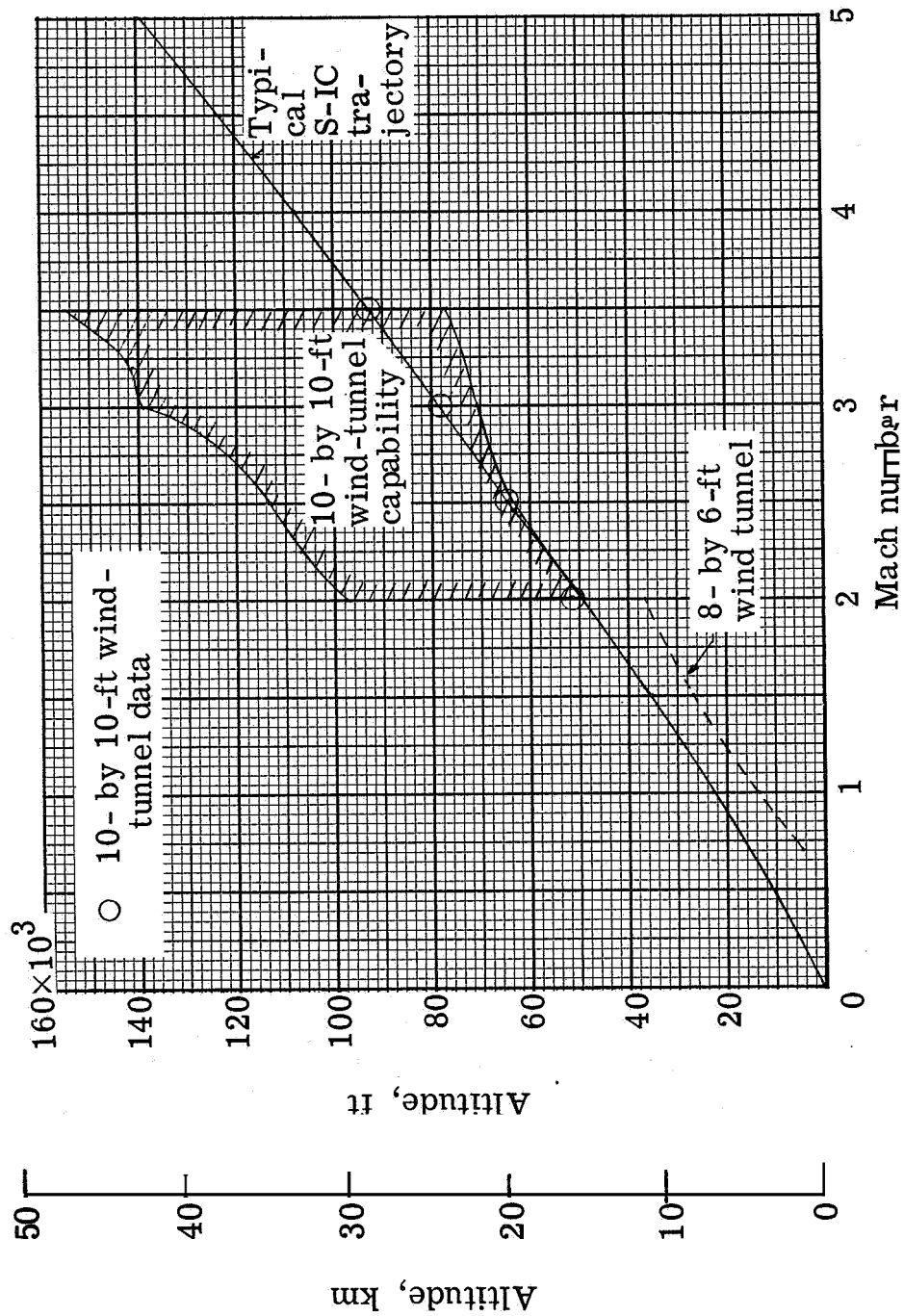


Figure 10 - Comparison of flight and wind-tunnel trajectories.

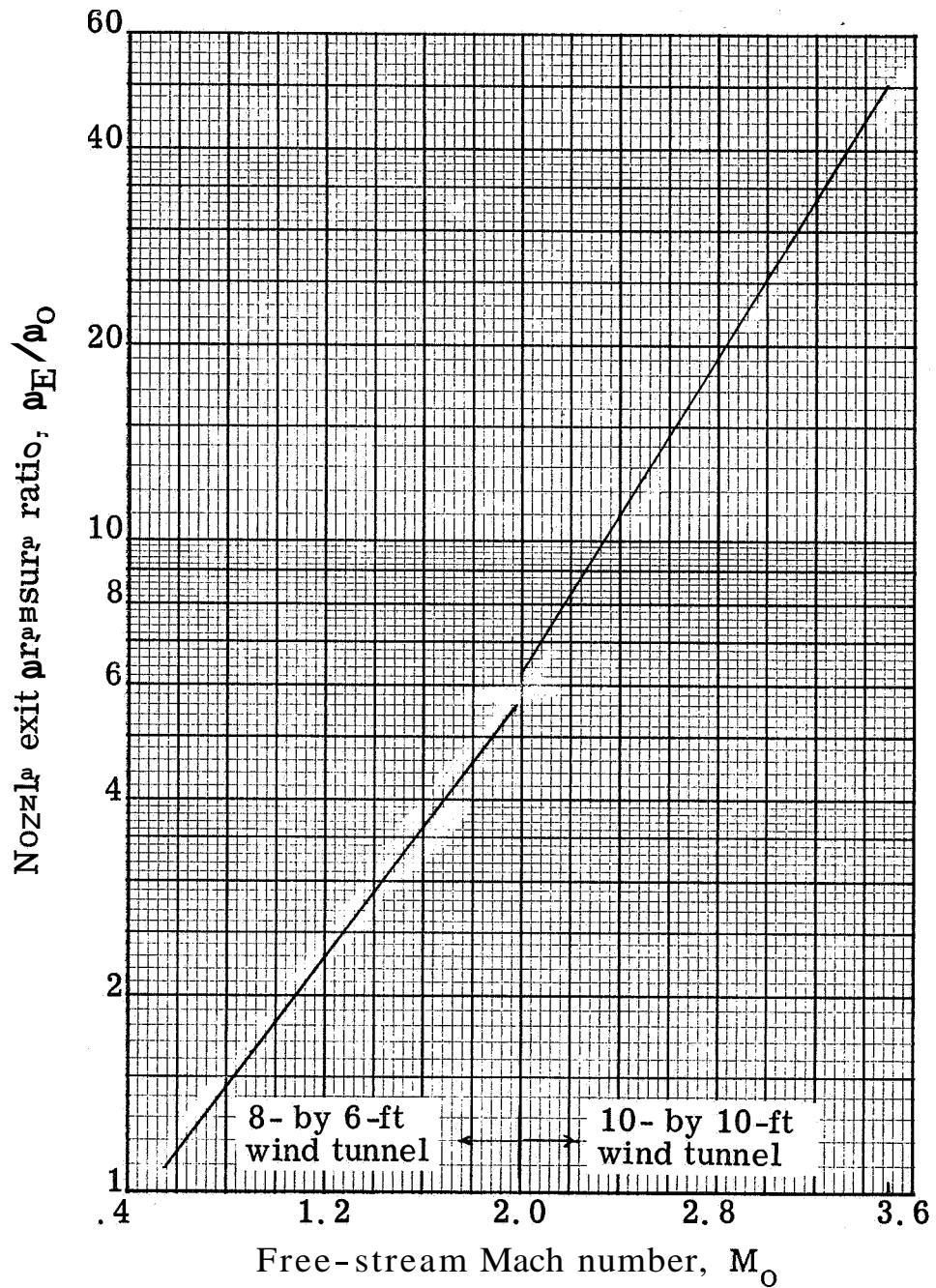
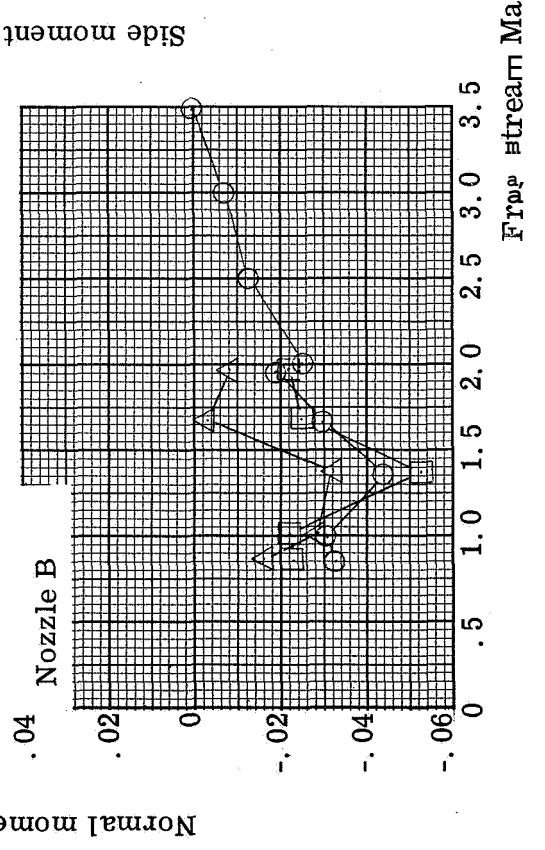
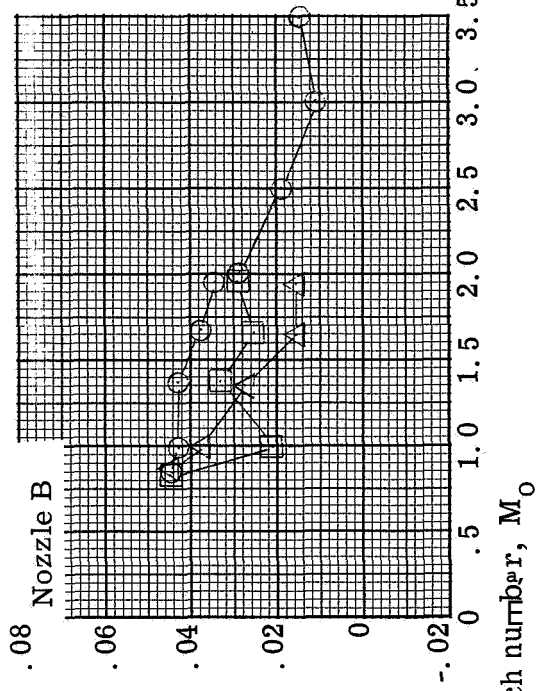
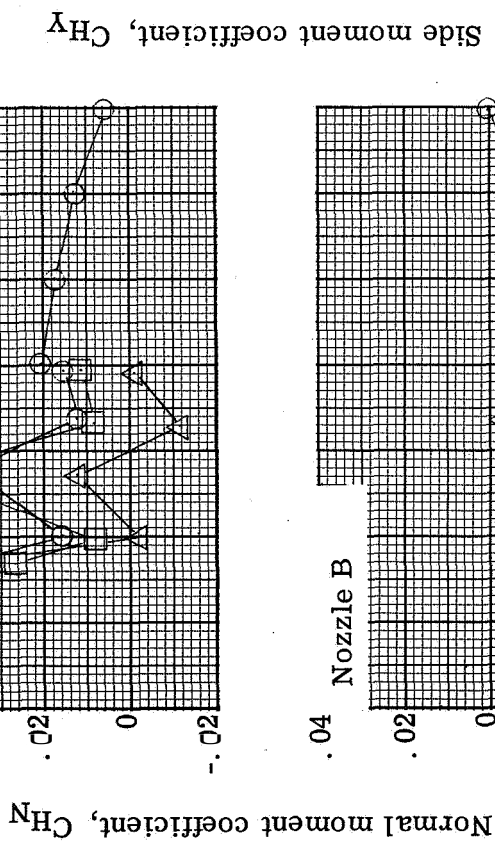
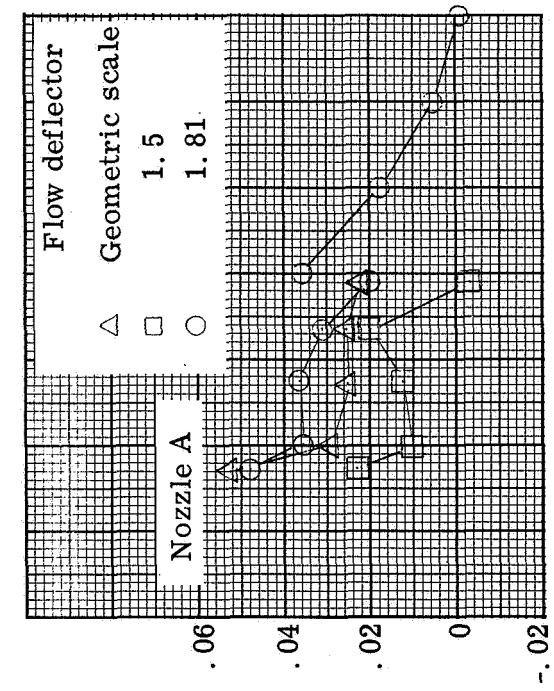
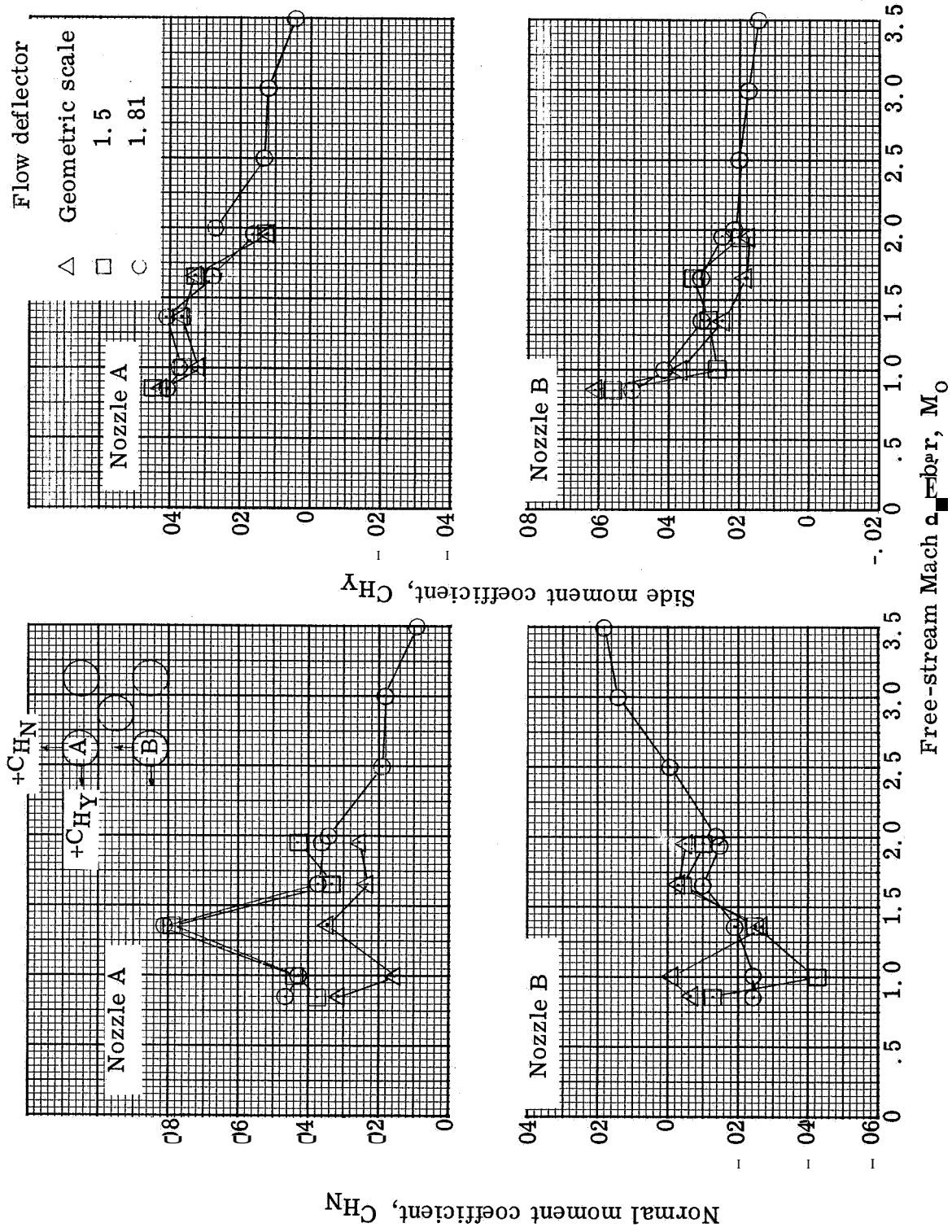


Figure 11. - Nozzle-exit-static-pressure-ratio trajectory.



(a) Nozzle gimbal angle 0°

Figure 12. - Effect of flow deflector on nozzle hinge moment at model angle $\alpha = 0^\circ$ and angle of attack $\alpha = 0^\circ$



(b) Nozzle gimbal angle, 3° .

Figure 12. - Concluded.

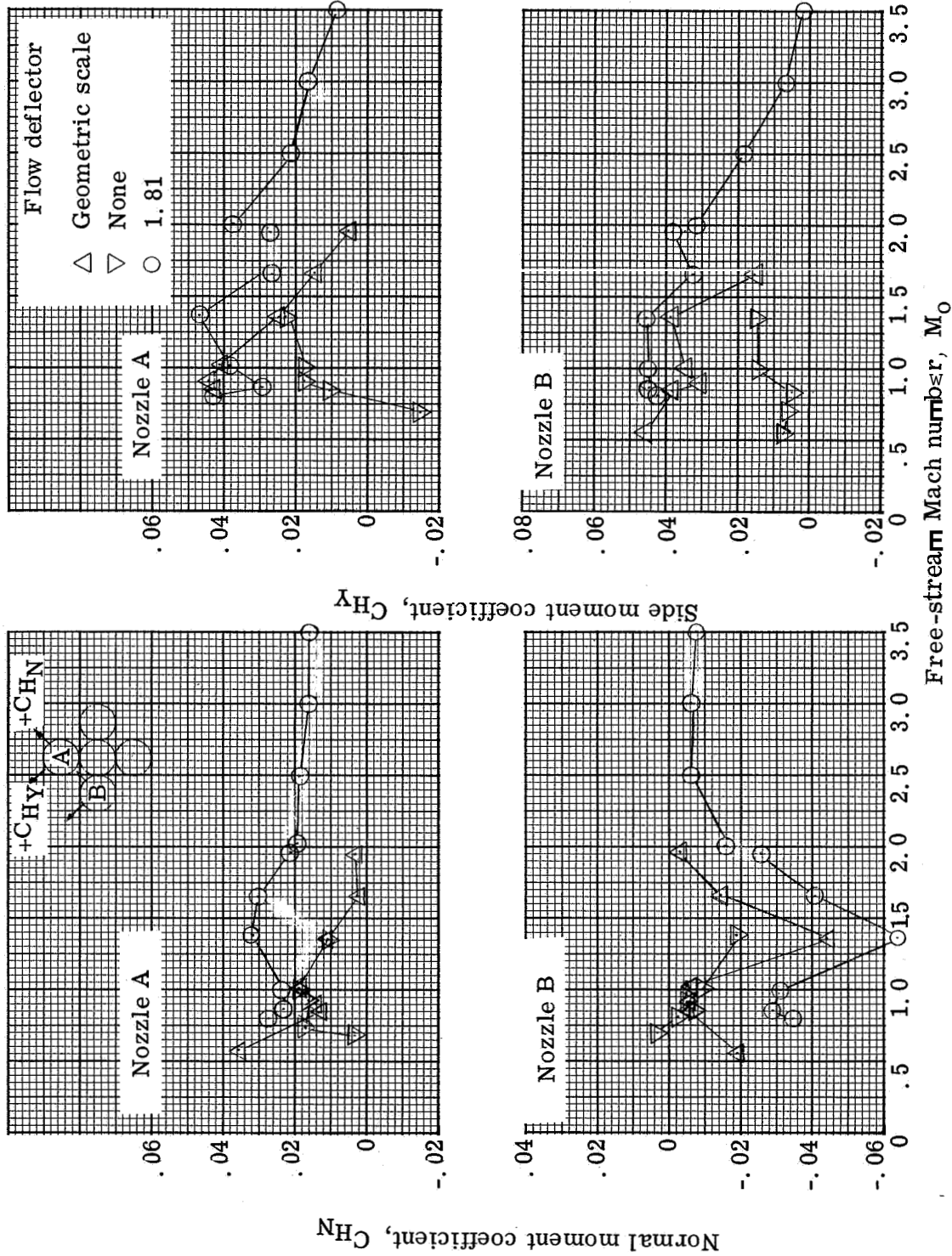
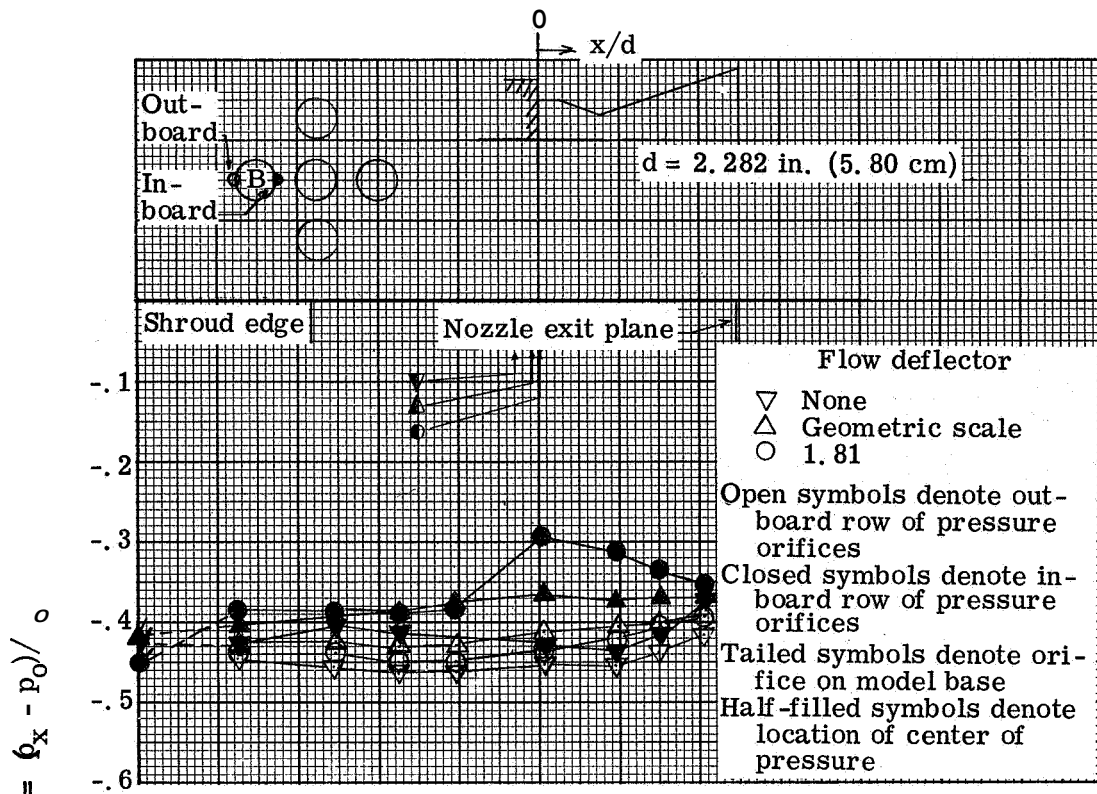
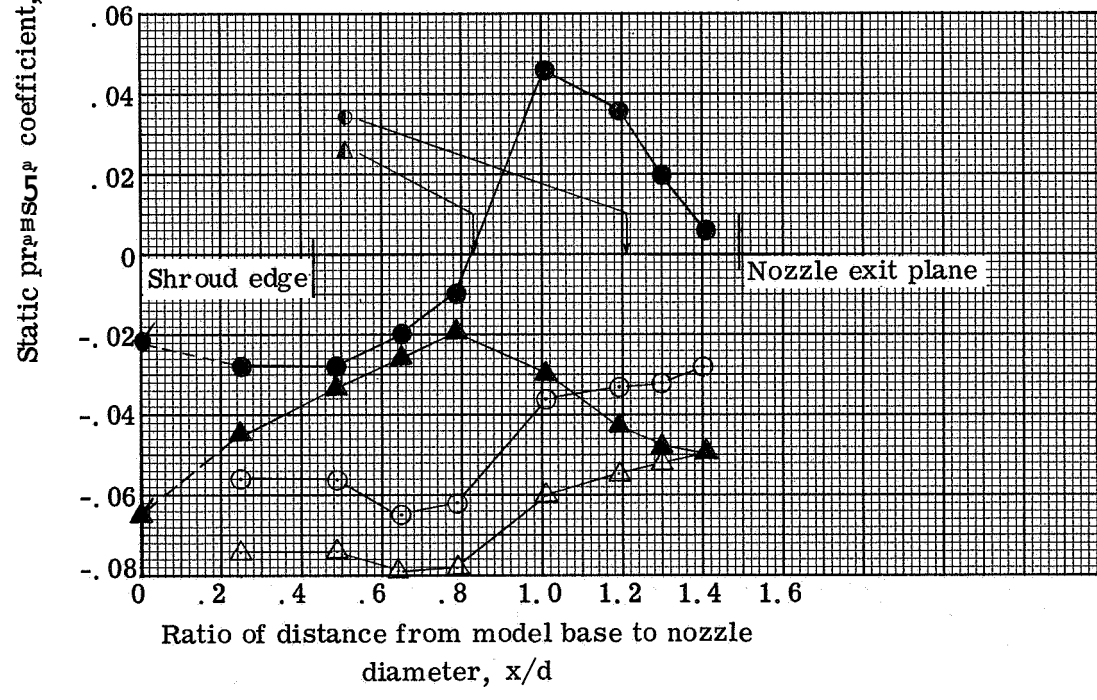


Figure 13. - Effect of flow deflectors on nozzle hinge moment at model roll angle of 45° , angle of attack of 0° , and nozzle gimbal angle of 0° .



(a) Nozzle-exit-pressure ratio, 1.95 ($M_0 = 1.0$).



(b) Nozzle-exit-pressure ratio, 3.65 ($M_0 = 1.66$).

Figure 14. - Effect of flow deflectors on nozzle static pressure distributions at 45° roll angle, 0° angle of attack, and 0° gimbal angle.

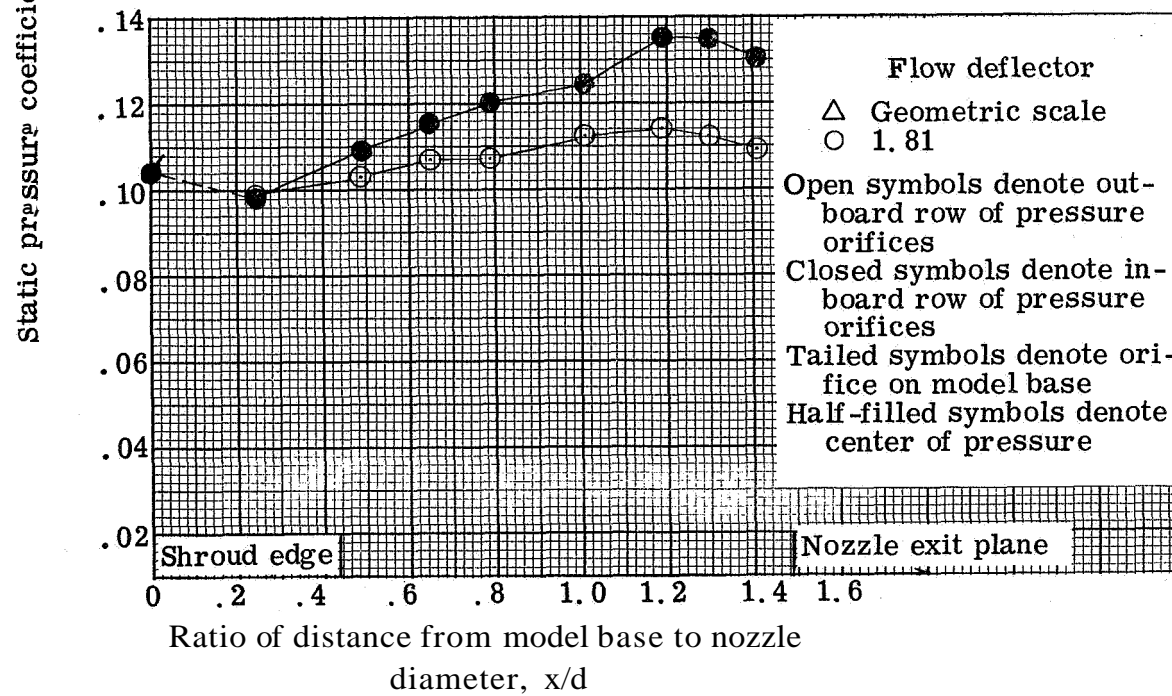
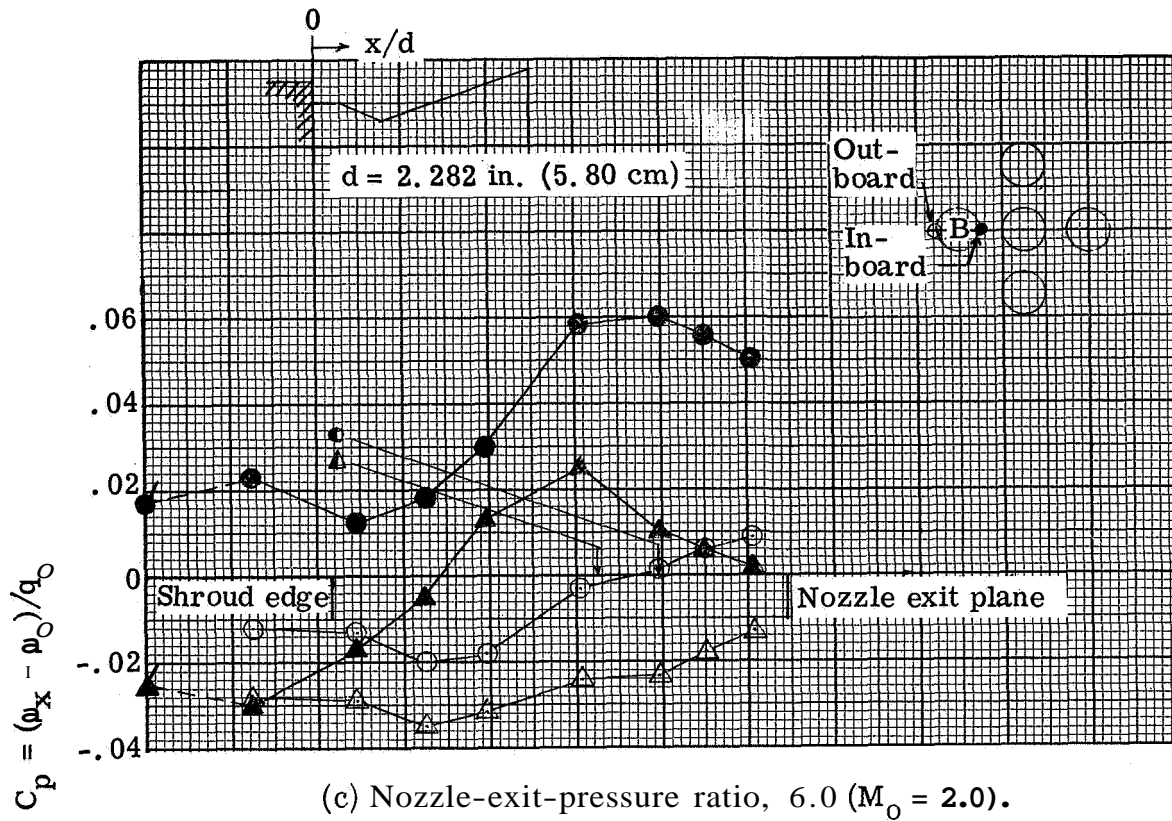
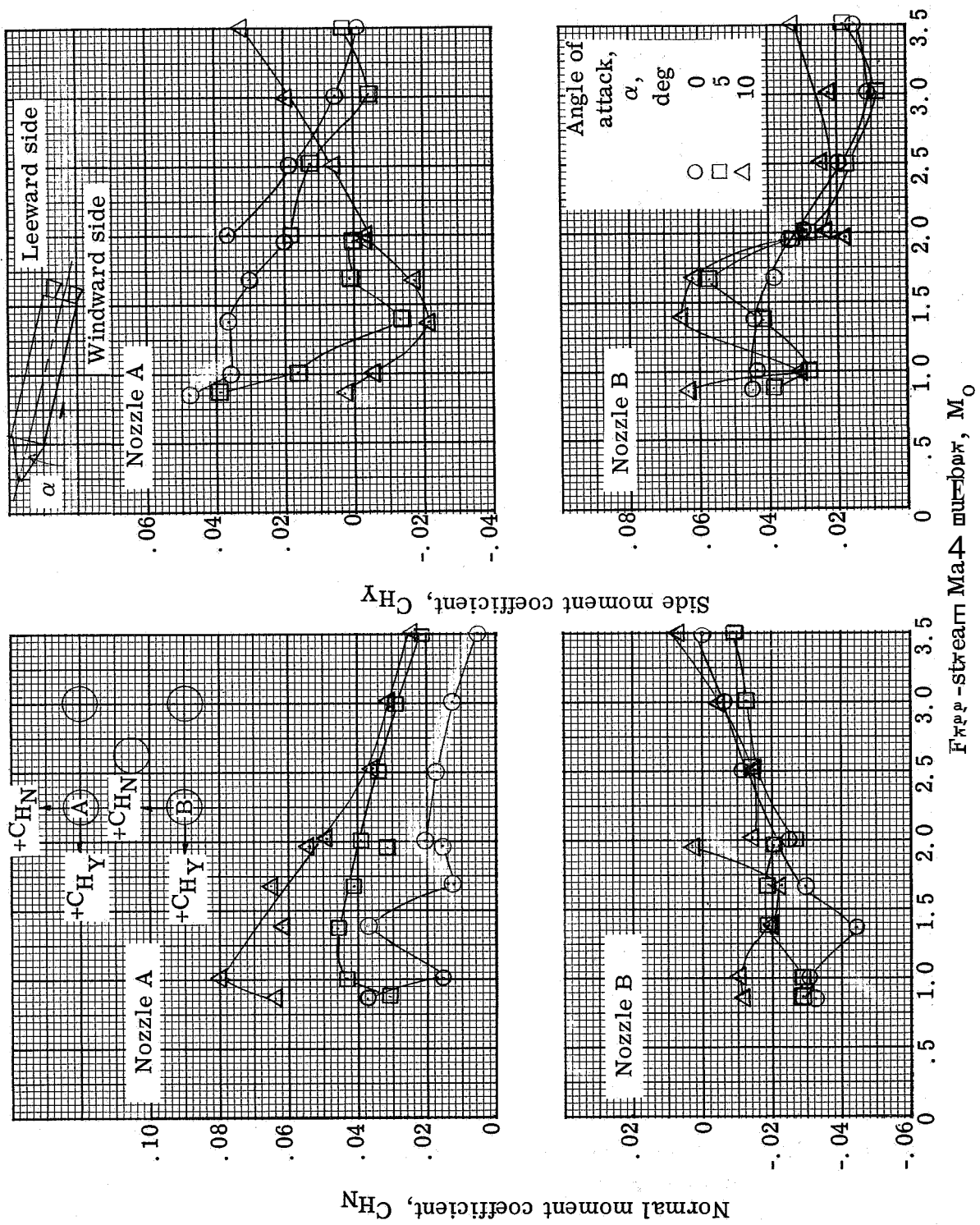
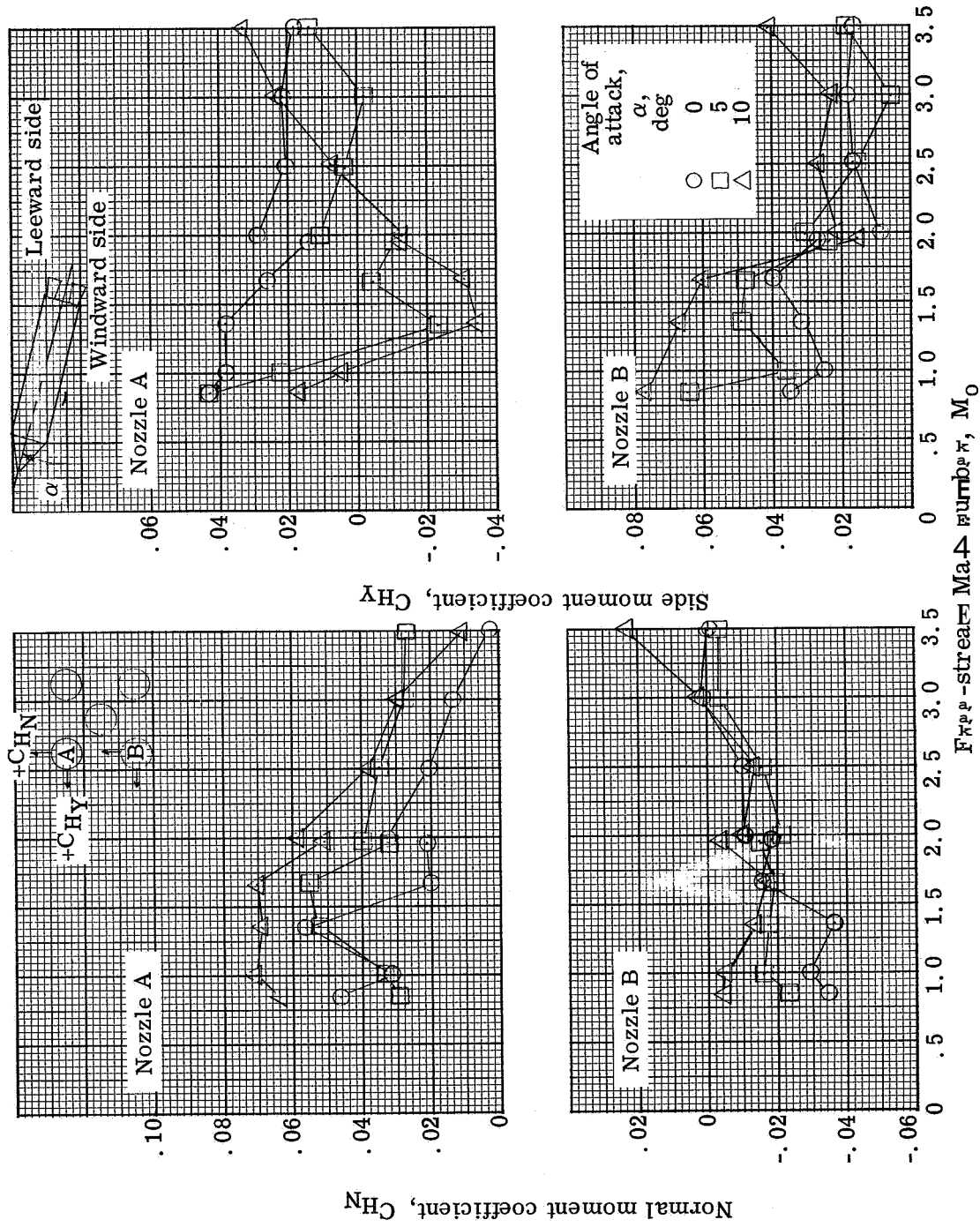


Figure 14. - Concluded.



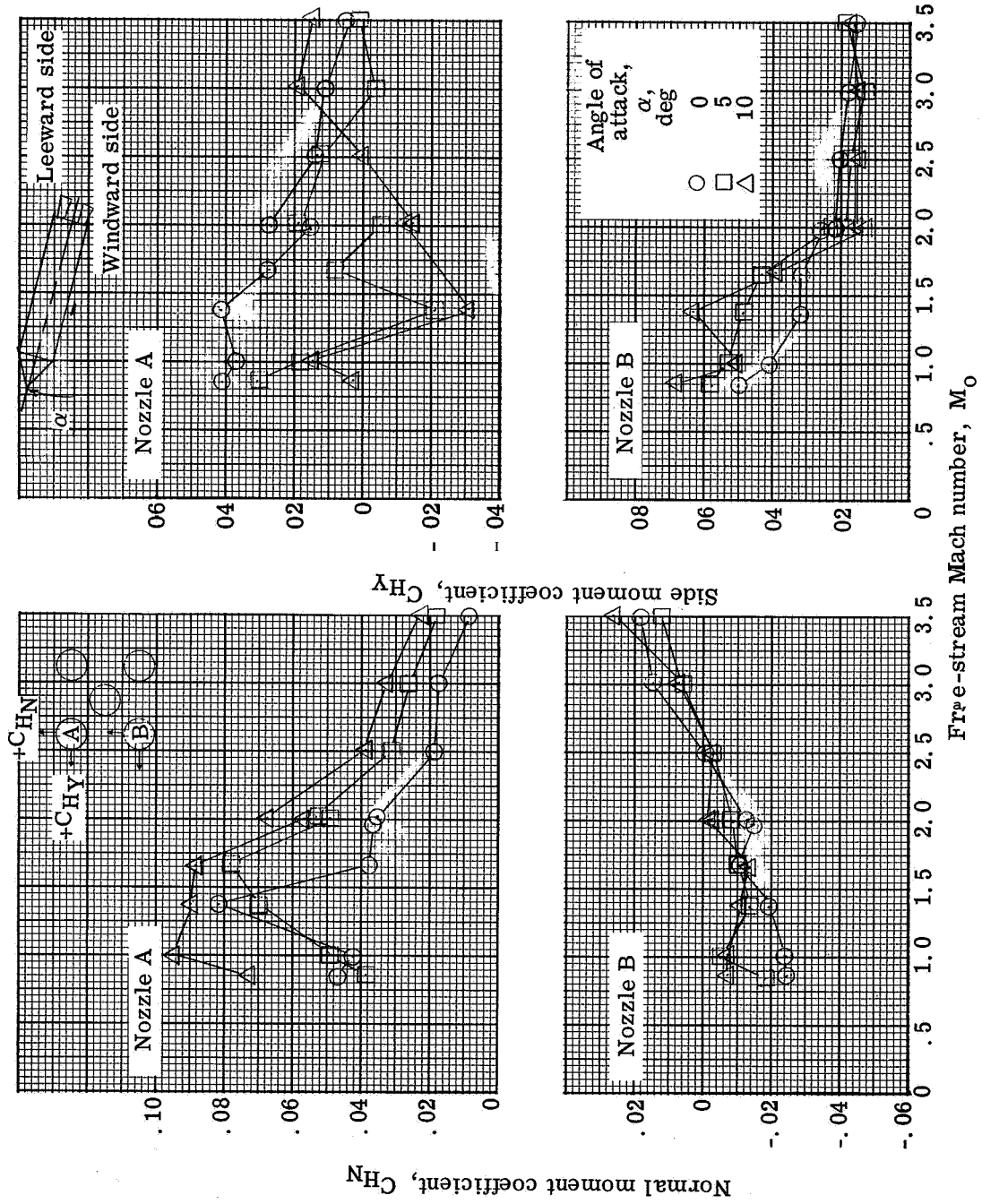
(a) Nozzle hinge moment at model angle of 0° with the 1.81 flow deflectors.

Figure 15. - Effect of angle of attack on nozzle hinge moment at model angle of 0° with the 1.81 flow deflectors.



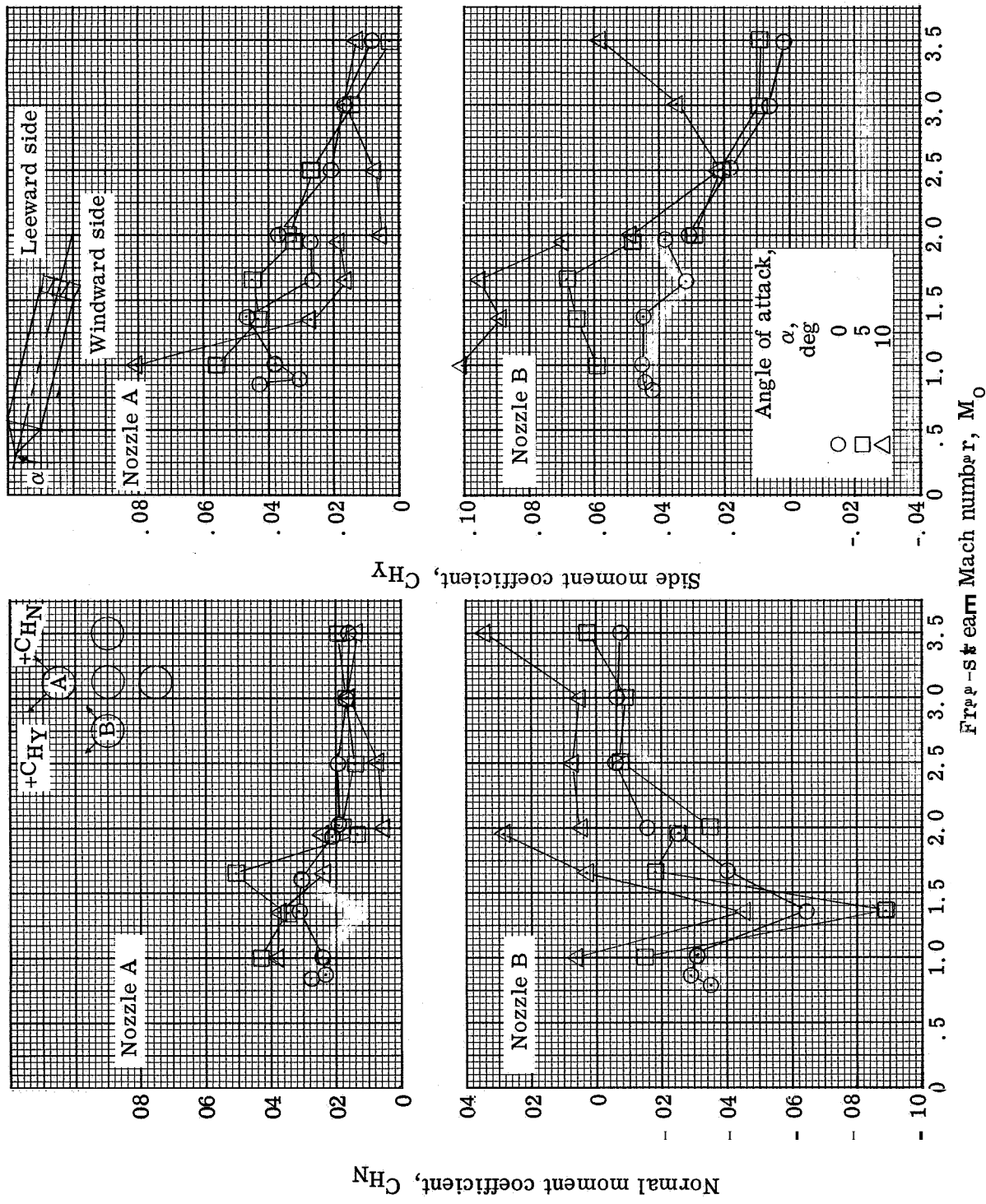
(D) Nozzle gimbal angle, 1.5°

Figure 15. - Continued



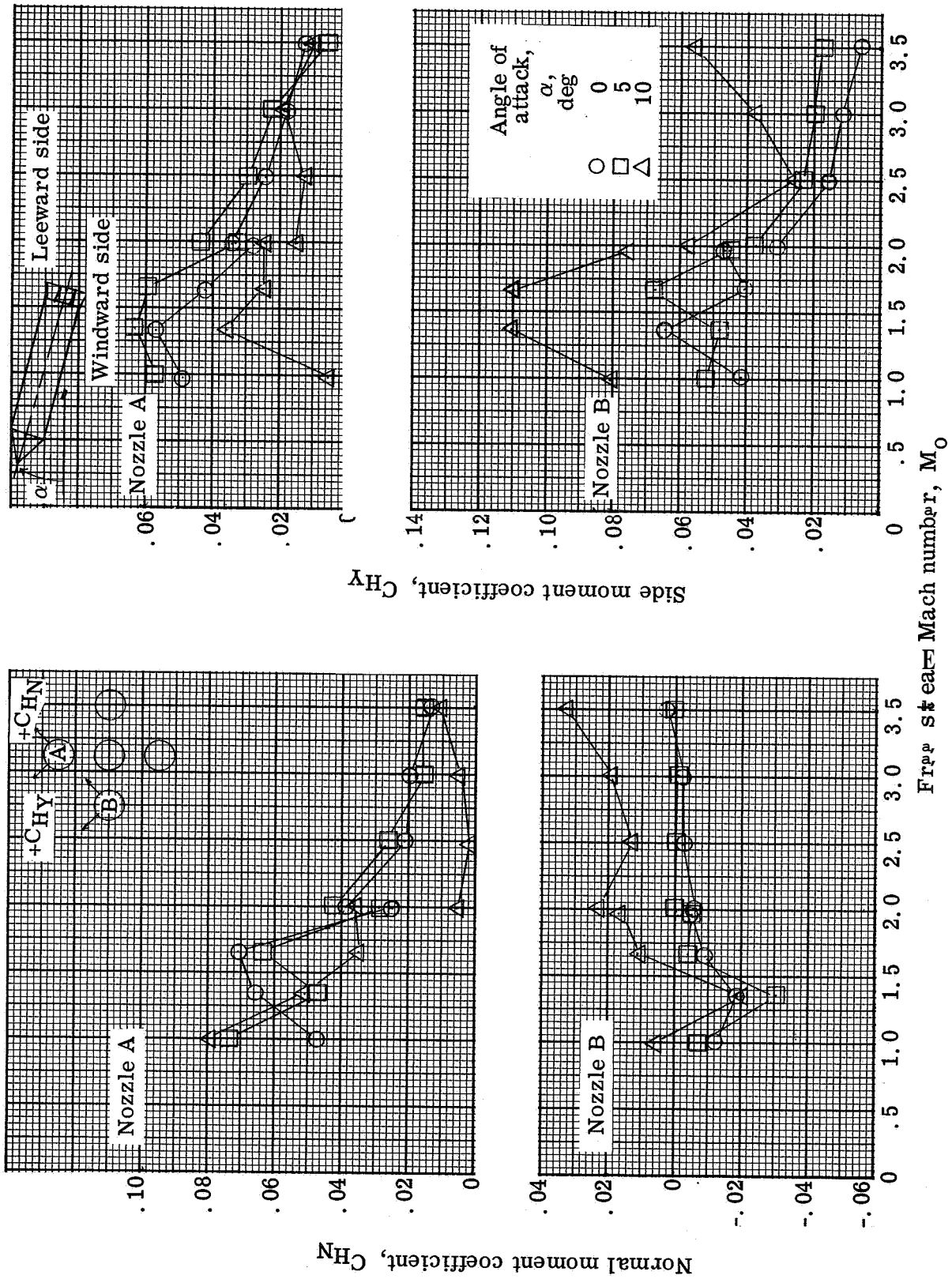
(c) Nozzle gimbal angle, 3°

Figure 15. - Concluded.



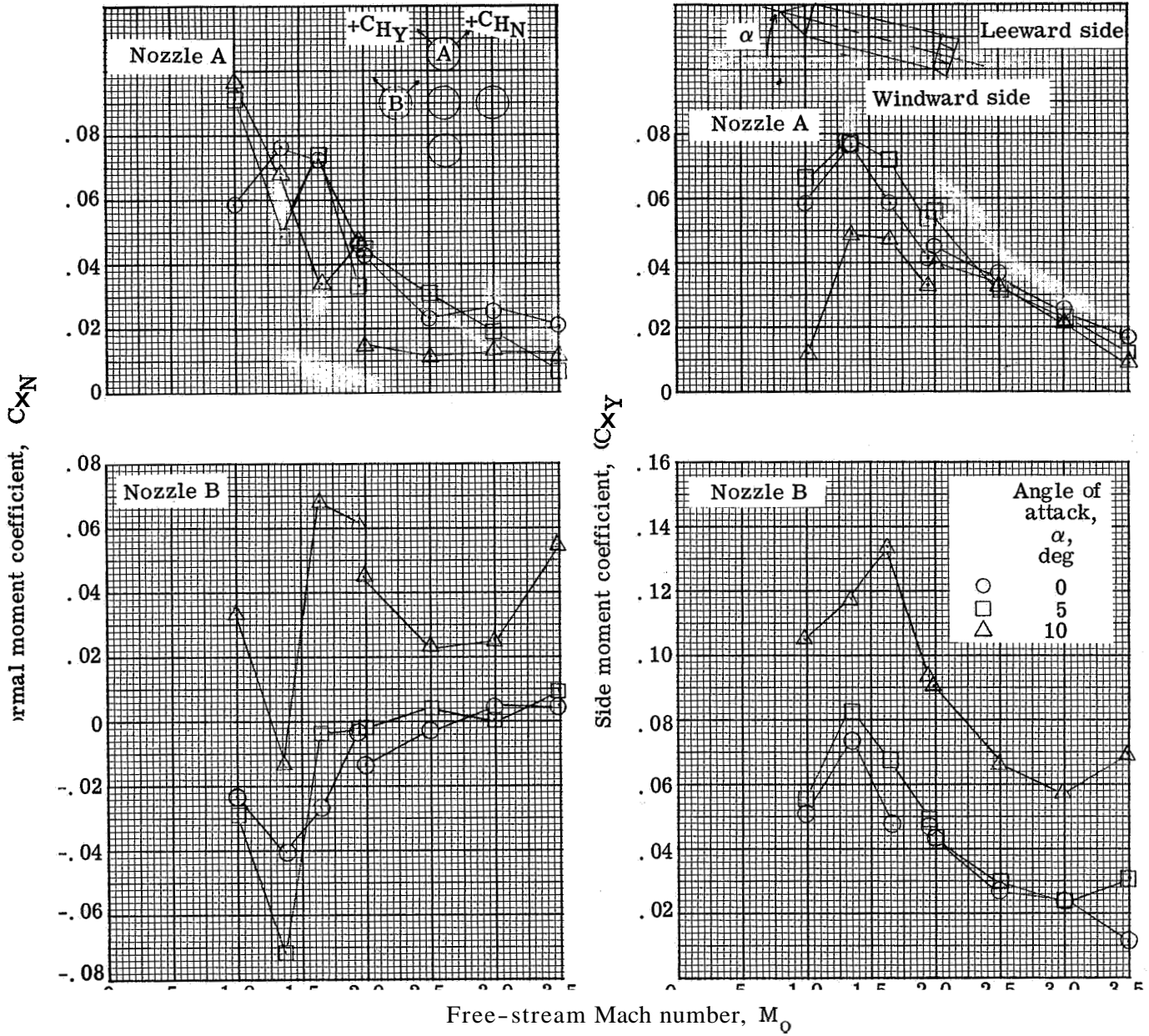
(a) Nozzle gimbal angle, 0°

Figure 16. - Effect of angle of attack on nozzle hinge moment at model roll angle of 45° with the 1.81 flow deflectors.



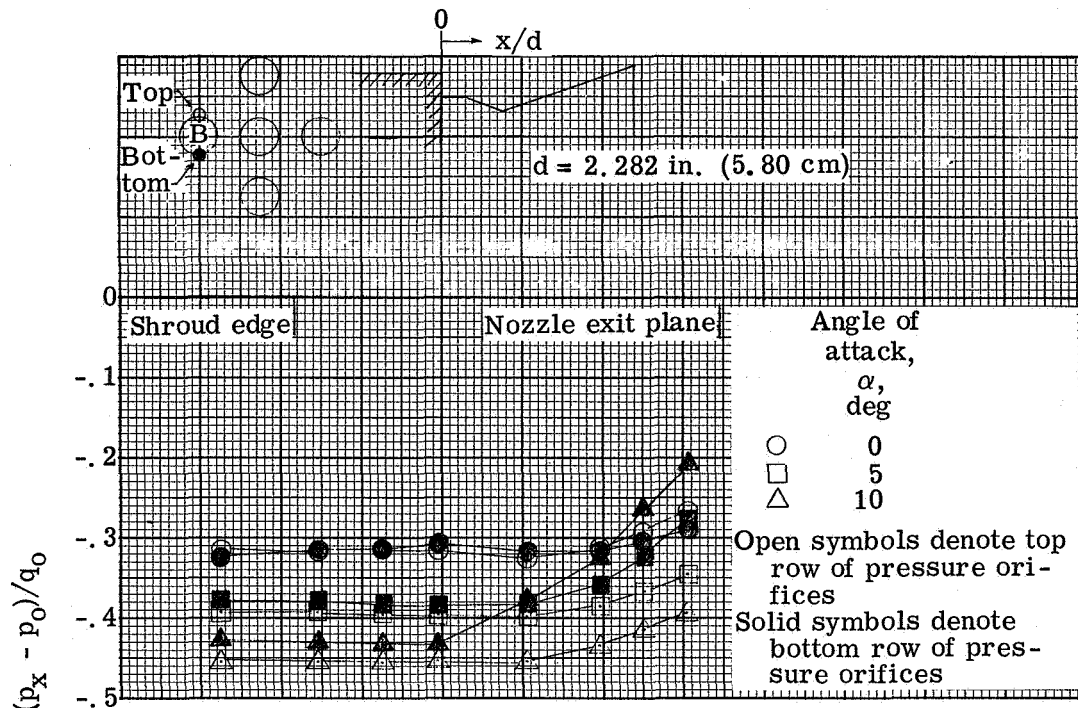
(D) Nozzle gimbal angle, 15°

Figure 1k - Continued.

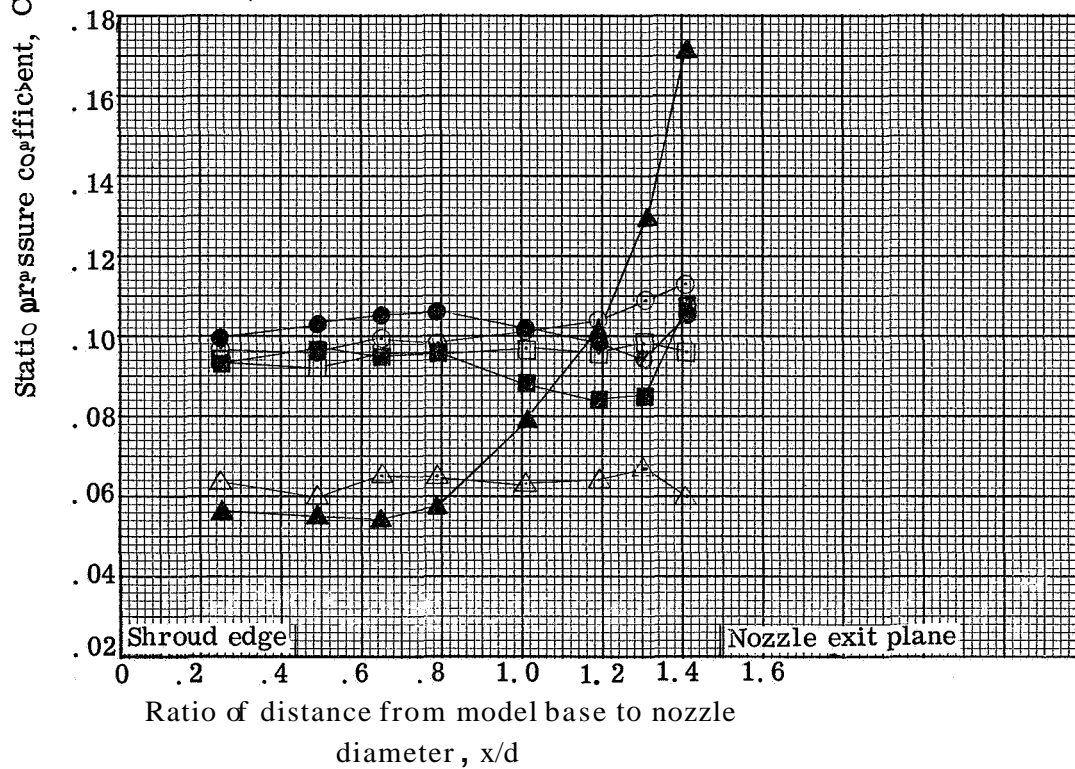


(c) Nozzle gimbal angle, 3° .

Figure 16. - Concluded.



(a) Nozzle-exit-pressure ratio, 2.6 ($M_0 = 1.0$).



(b) Nozzle-exit-pressure ratio, 25.5 ($M_0 = 3.0$).

Figure 17. - Effect of angle of attack on nozzle static pressure distribution at 45° roll angle and 0° gimbal angle with the 1.81 flow deflectors.

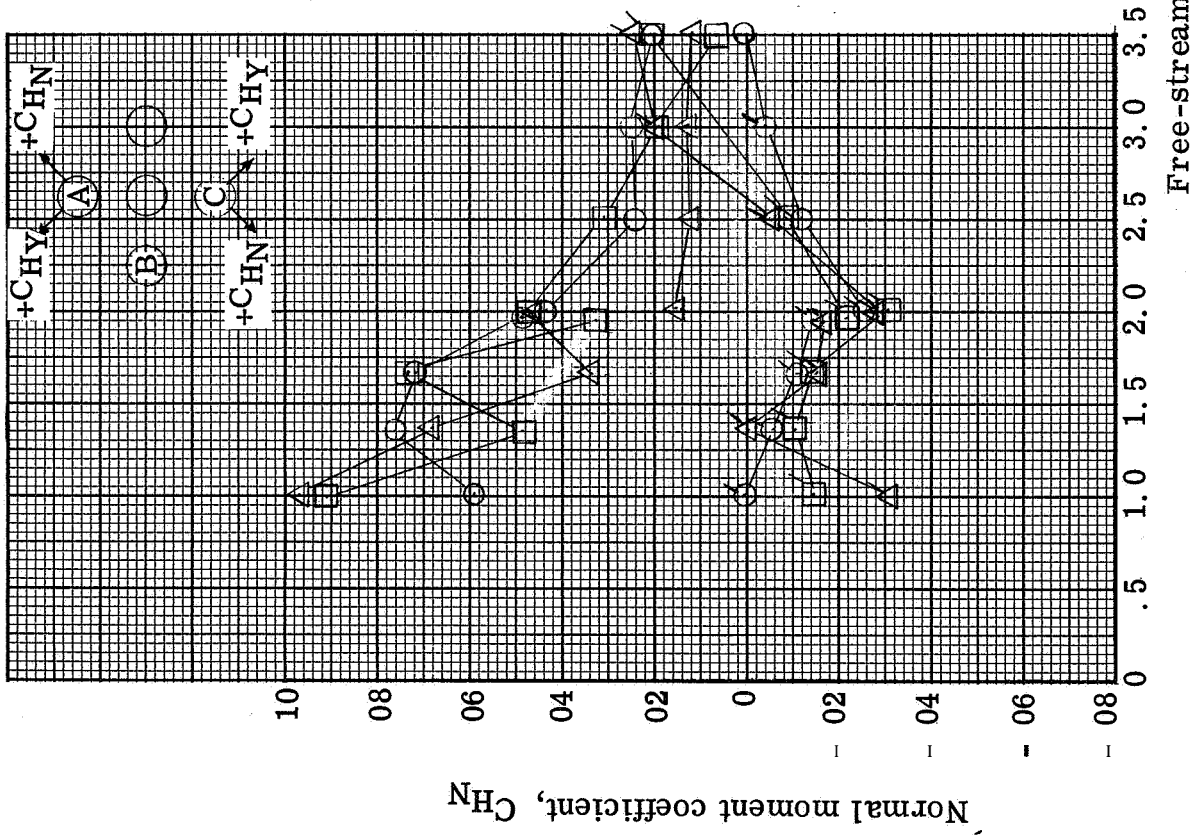
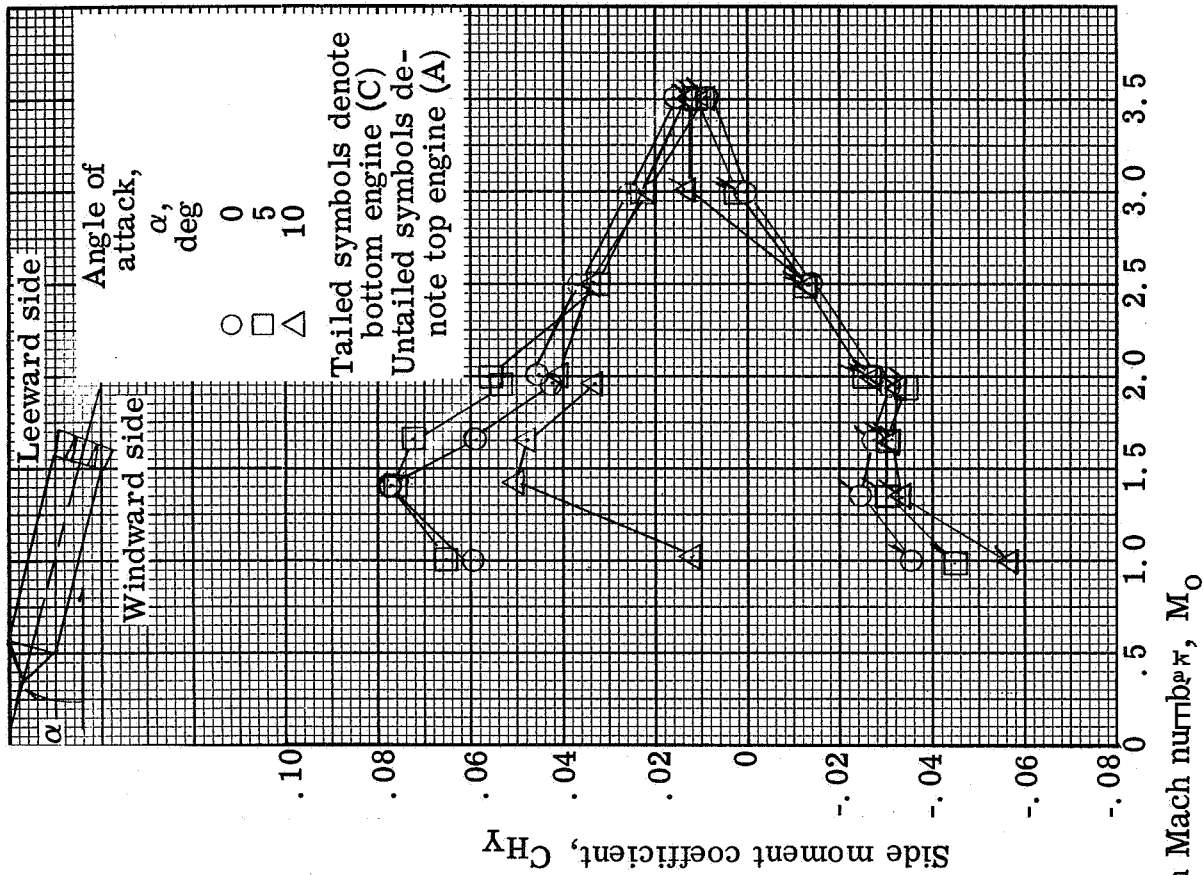
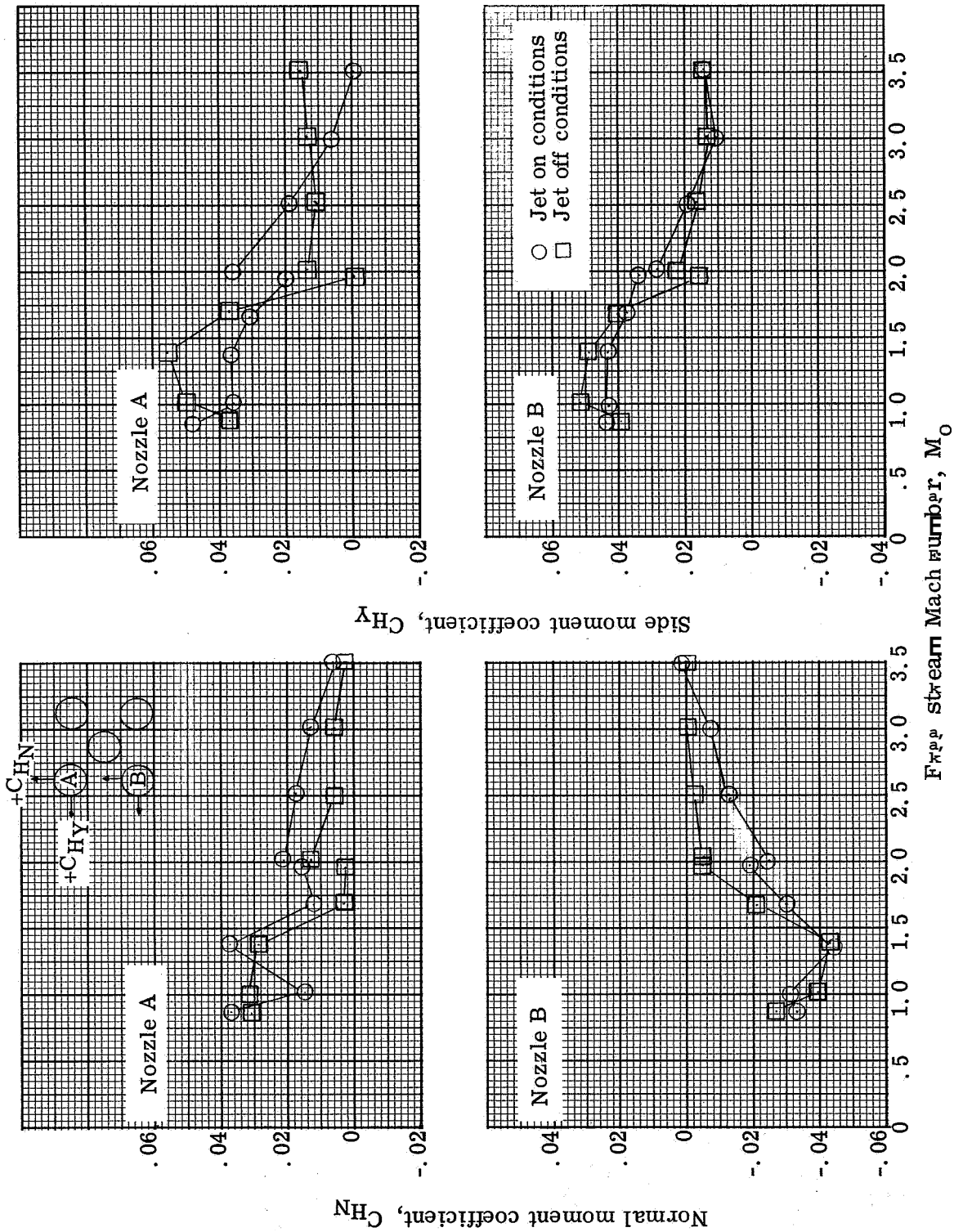
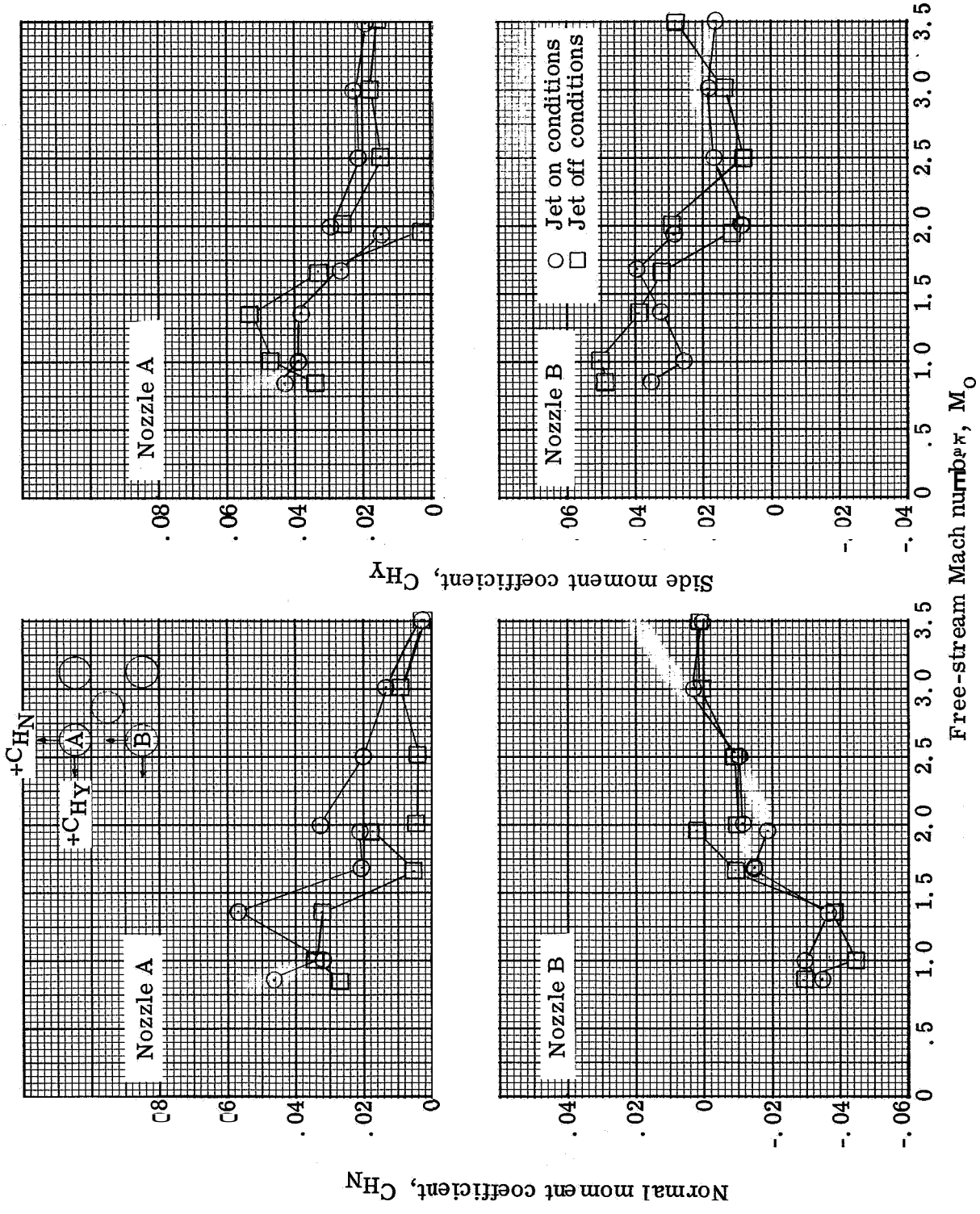


Figure 18. - Comparison of hinge moment data between top and bottom engines at M_0 of 45° and nozzle gimbal angle of 3° with the 1.81 flow deflectors.



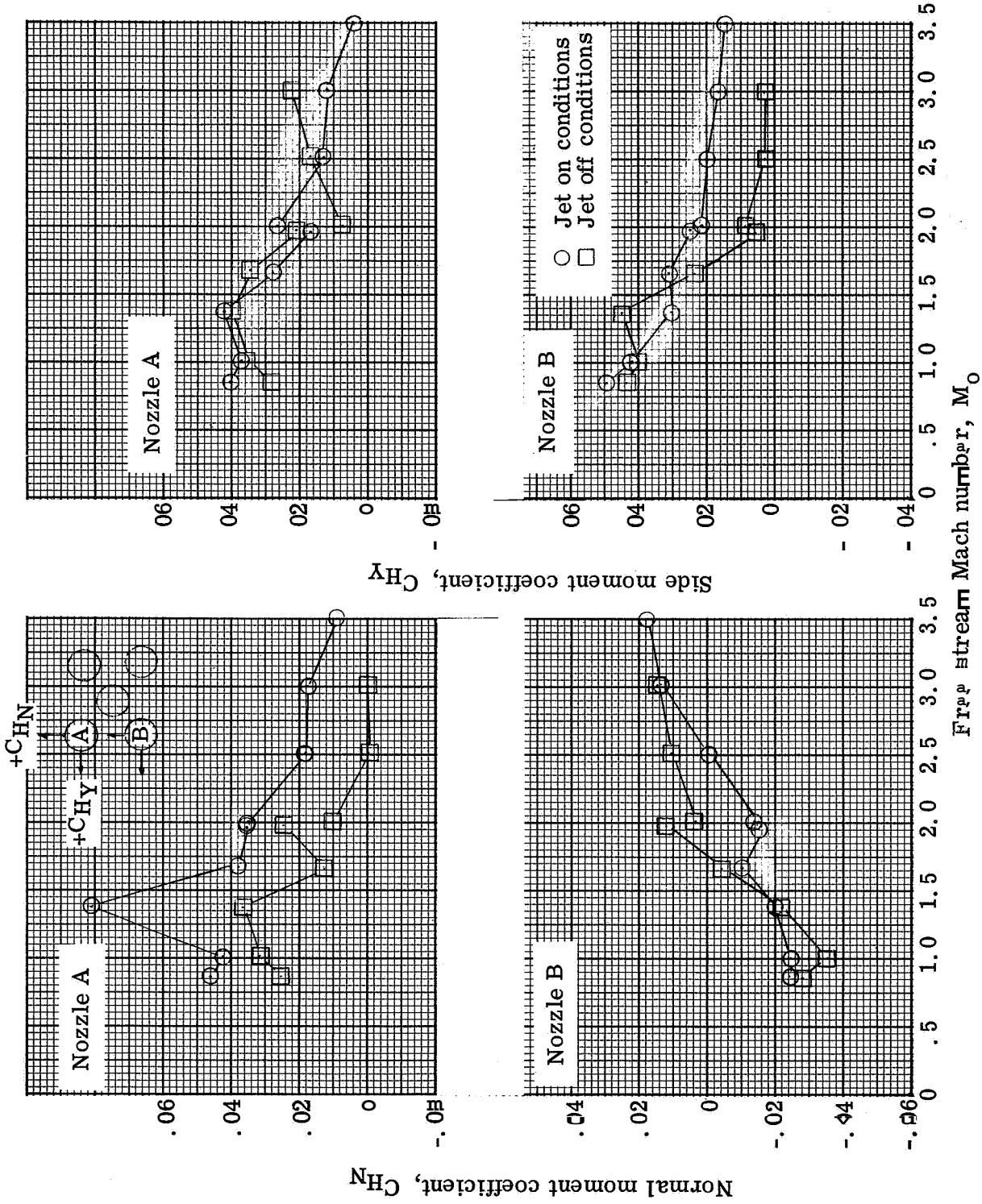
(a) Nozzle gimbal angle, 0°

Figure 19. - Comparison of nozzle hinge-moment coefficients with jet-on and jet-off conditions at model roll angle of 0° and angle of attack of 0° with the 1.81 flow deflectors.



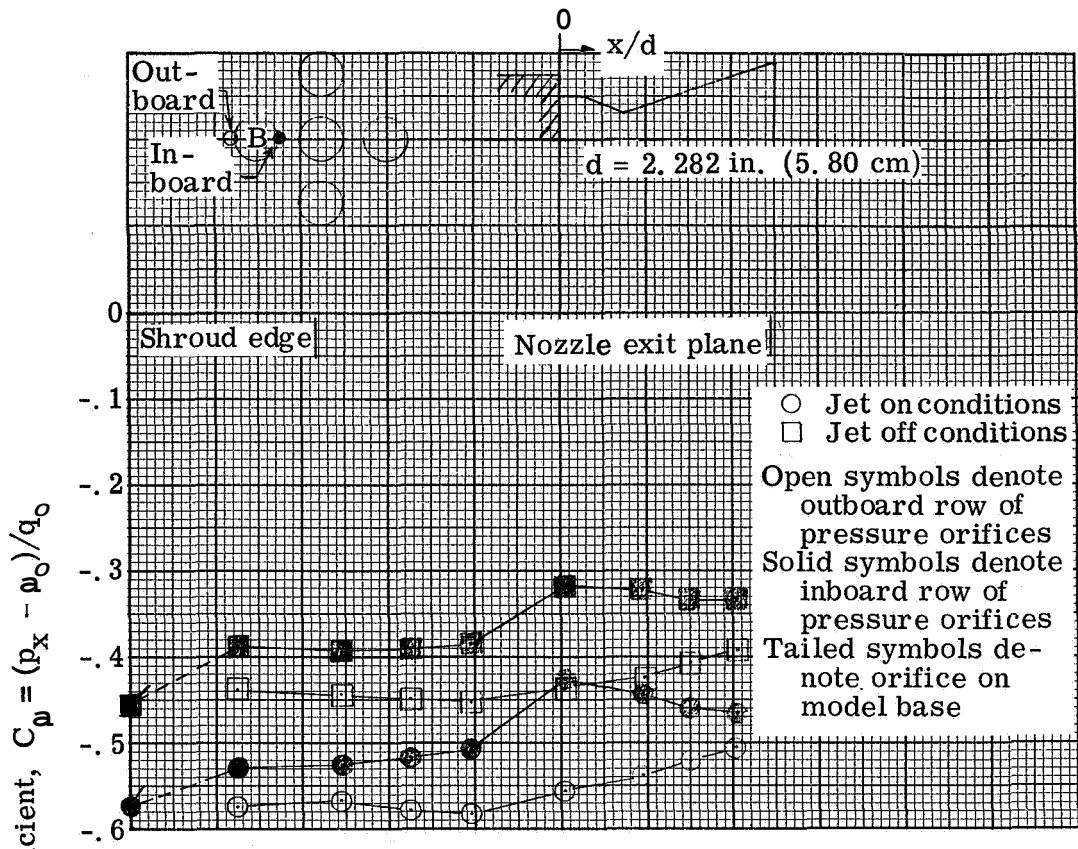
(D) Nozzle gimbal angle, 1.5°.

Figure 19. - Continued.

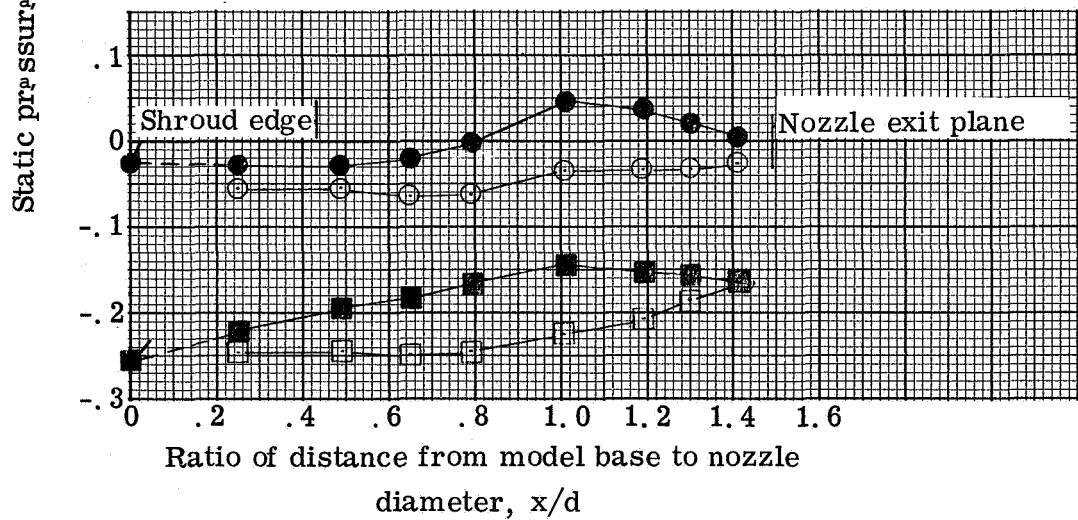


(c) Nozzle gimballed angle, 3°

Figure 19. - Contd.

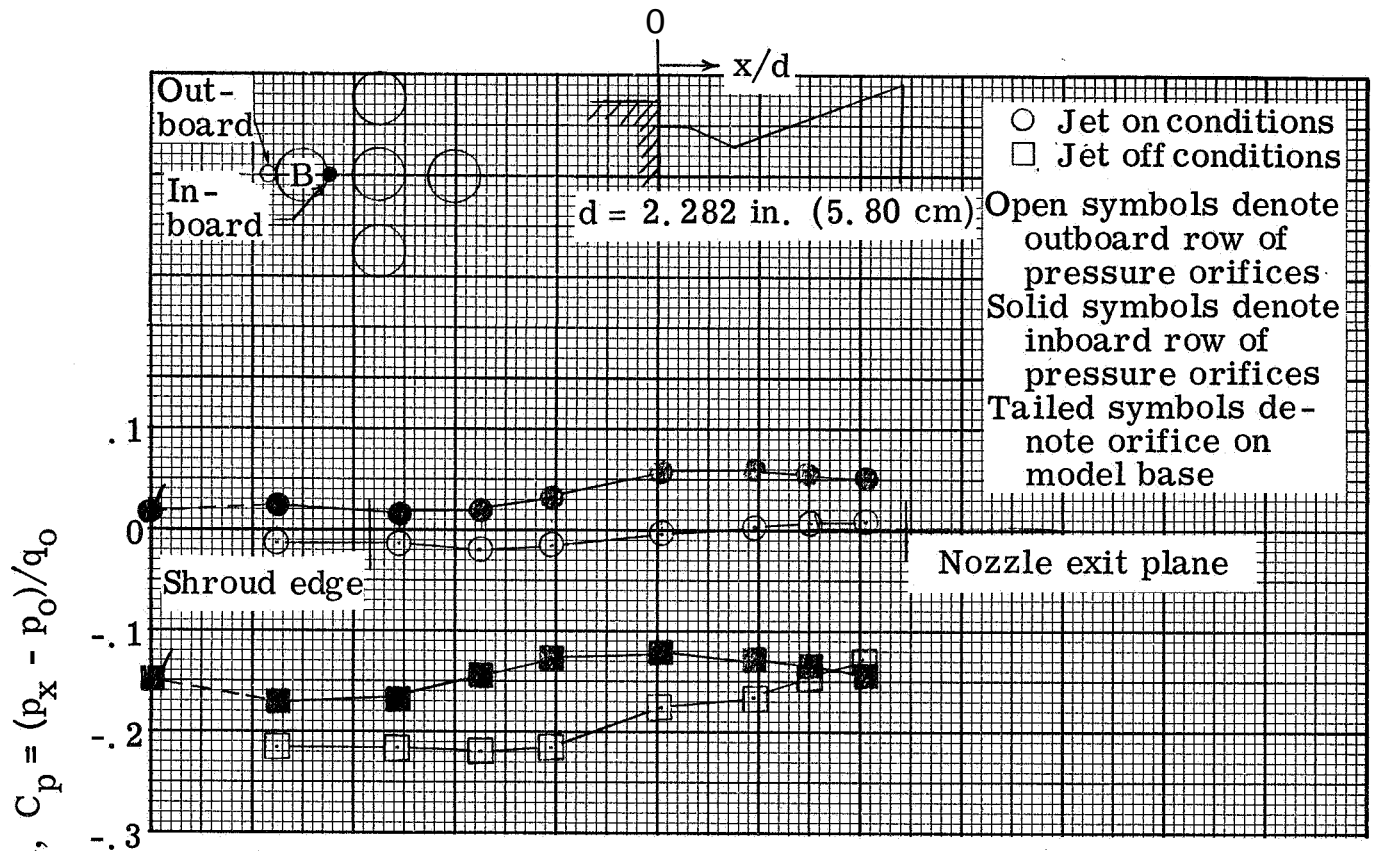


(a) Nozzle-exit-pressure ratio, 1.17 ($M_o = 1.0$).

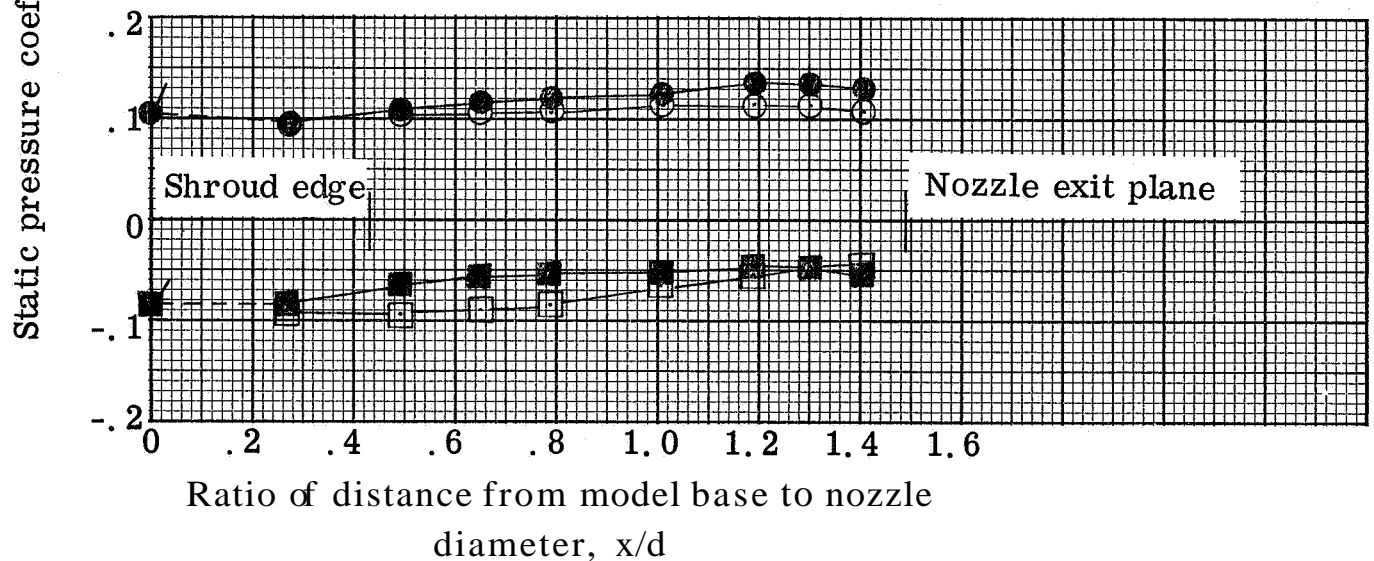


(b) Nozzle-exit-pressure ratio, 3.65 ($M_o = 1.66$).

Figure 20. - Comparison of nozzle-static-pressure distributions with jet-on and jet-off conditions at 45° roll angle, 0° angle of attack, and 0° gimbal angle with the 1.81 flow deflectors.

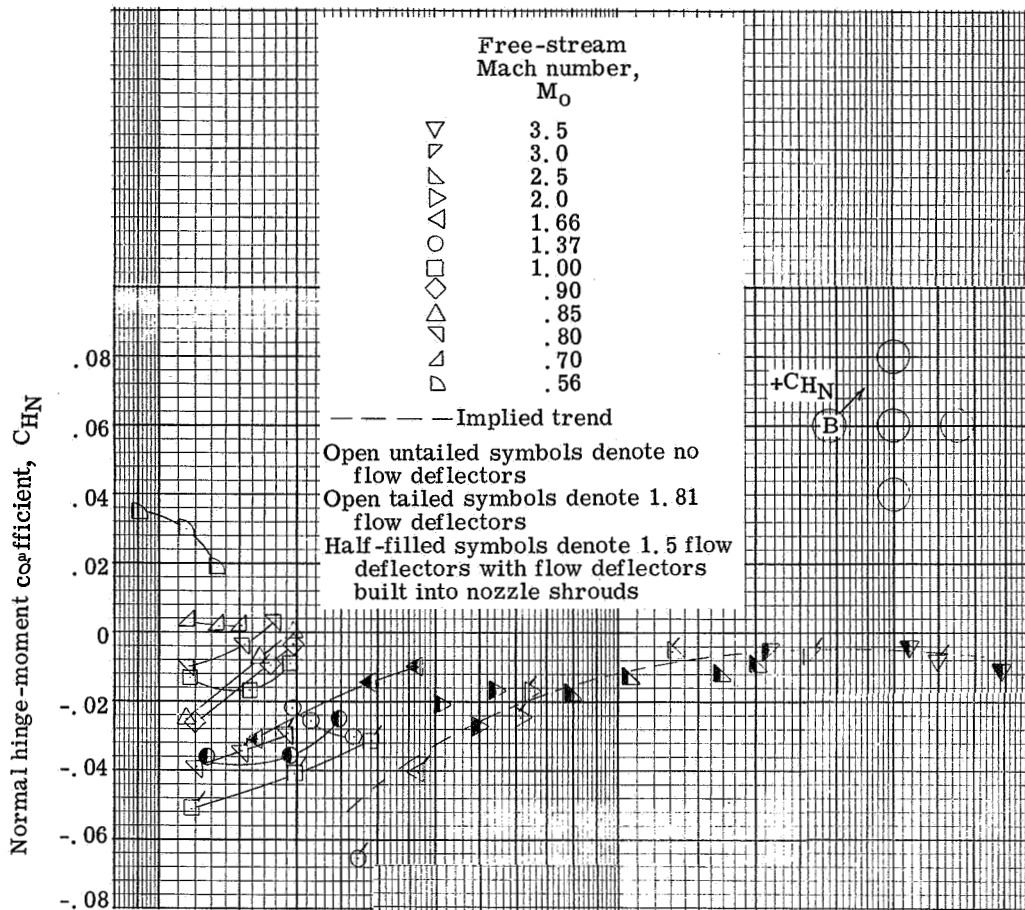


(c) Nozzle-exit-pressure ratio, 6.0 ($M_0 = 2.0$).

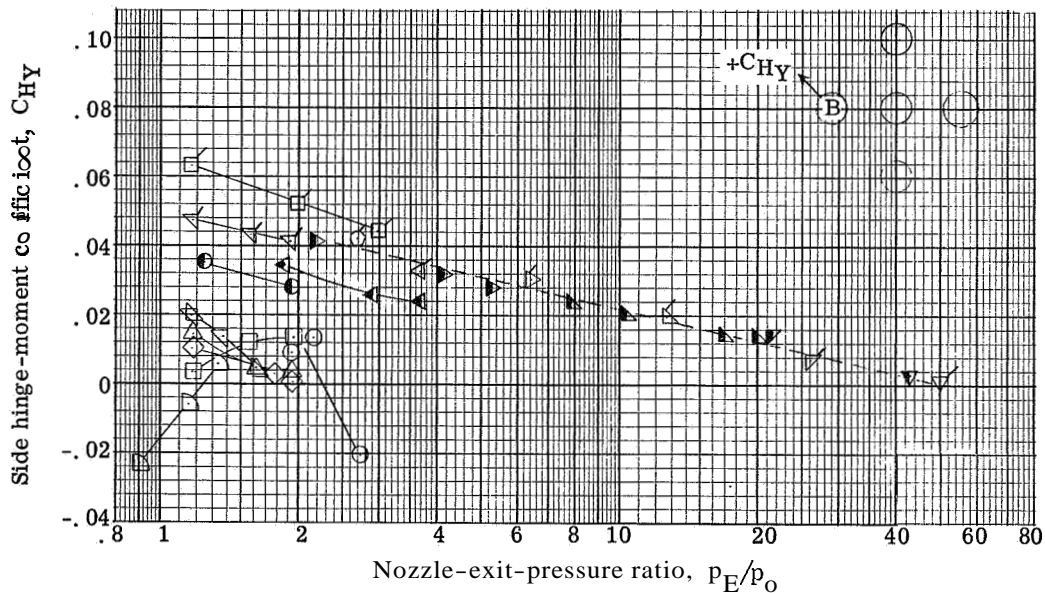


(d) Nozzle-exit-pressure ratio, 25.5 ($M_0 = 3.0$).

Figure 20. - Concluded.



(a) Normal hinge-moment coefficient.



(b) Side hinge-moment coefficient.

Figure 21. - Effect of nozzle pressure ratio on nozzle hinge moment for nozzle B at 45° roll angle, 0° angle of attack, and 0° gimbal angle.

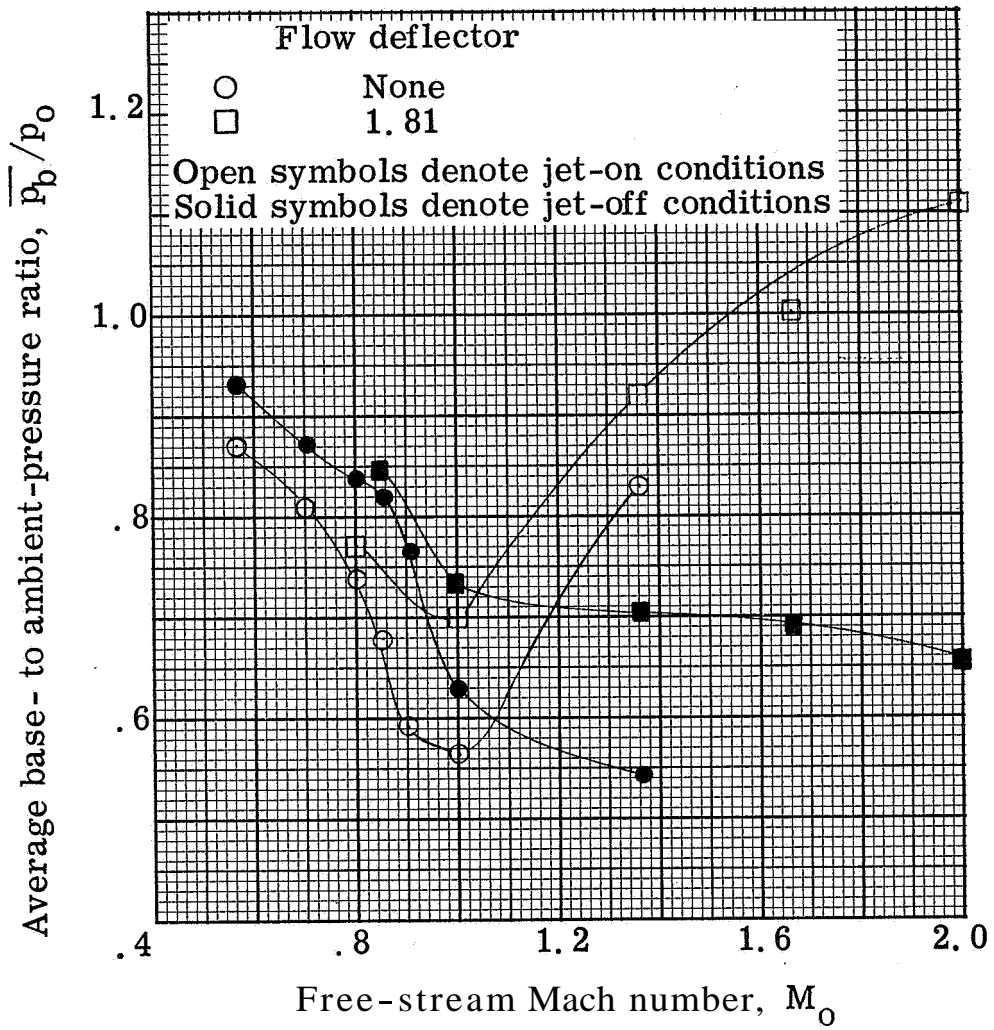


Figure 22. - Jet effects on average base pressure ratio. Model roll angle; 45° .

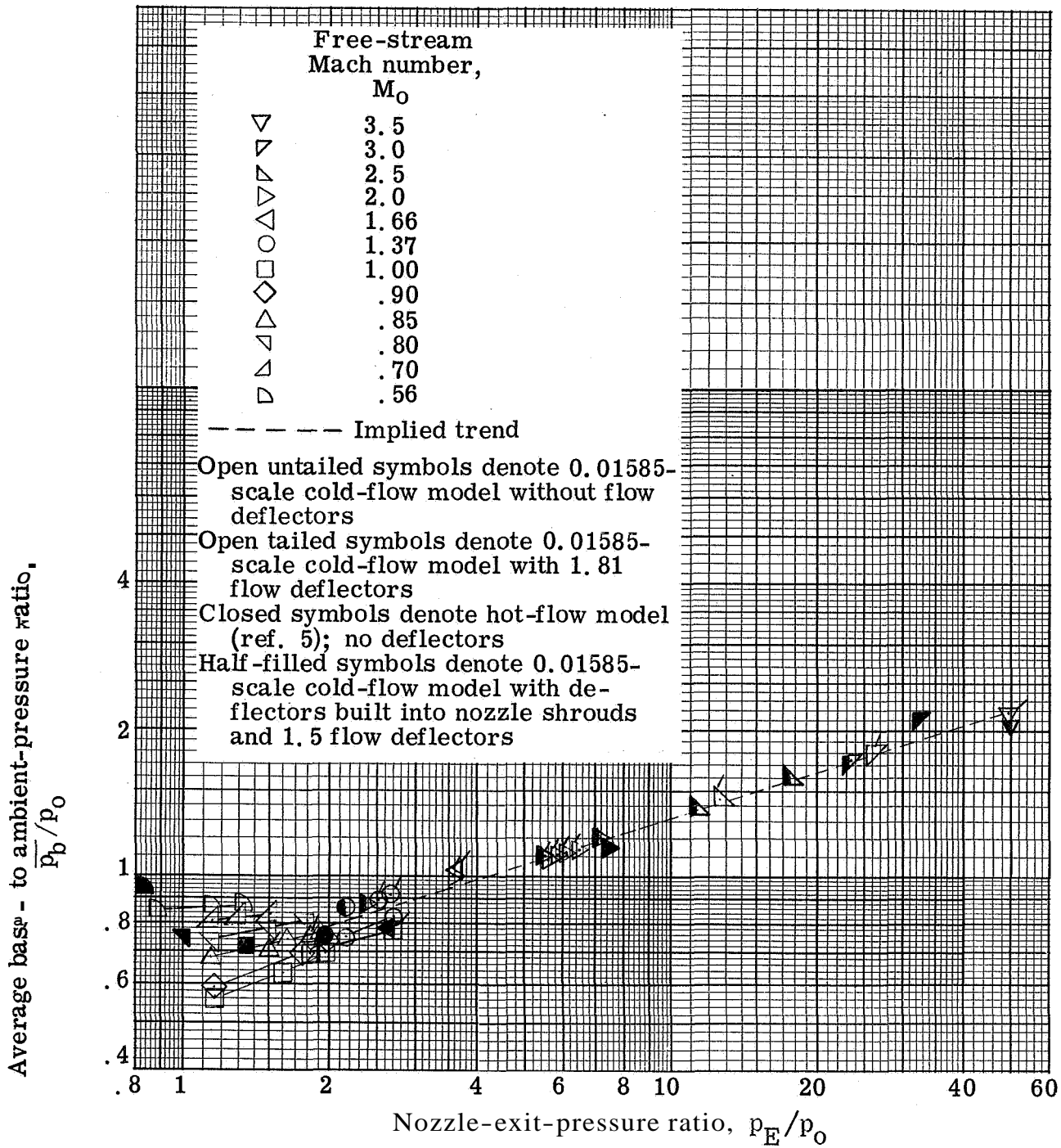


Figure 23. - Average base pressure ratio as function of nozzle-exit-pressure ratio at model roll angle of 45° , gimbal angle of 0° , and angle of attack of 0° .

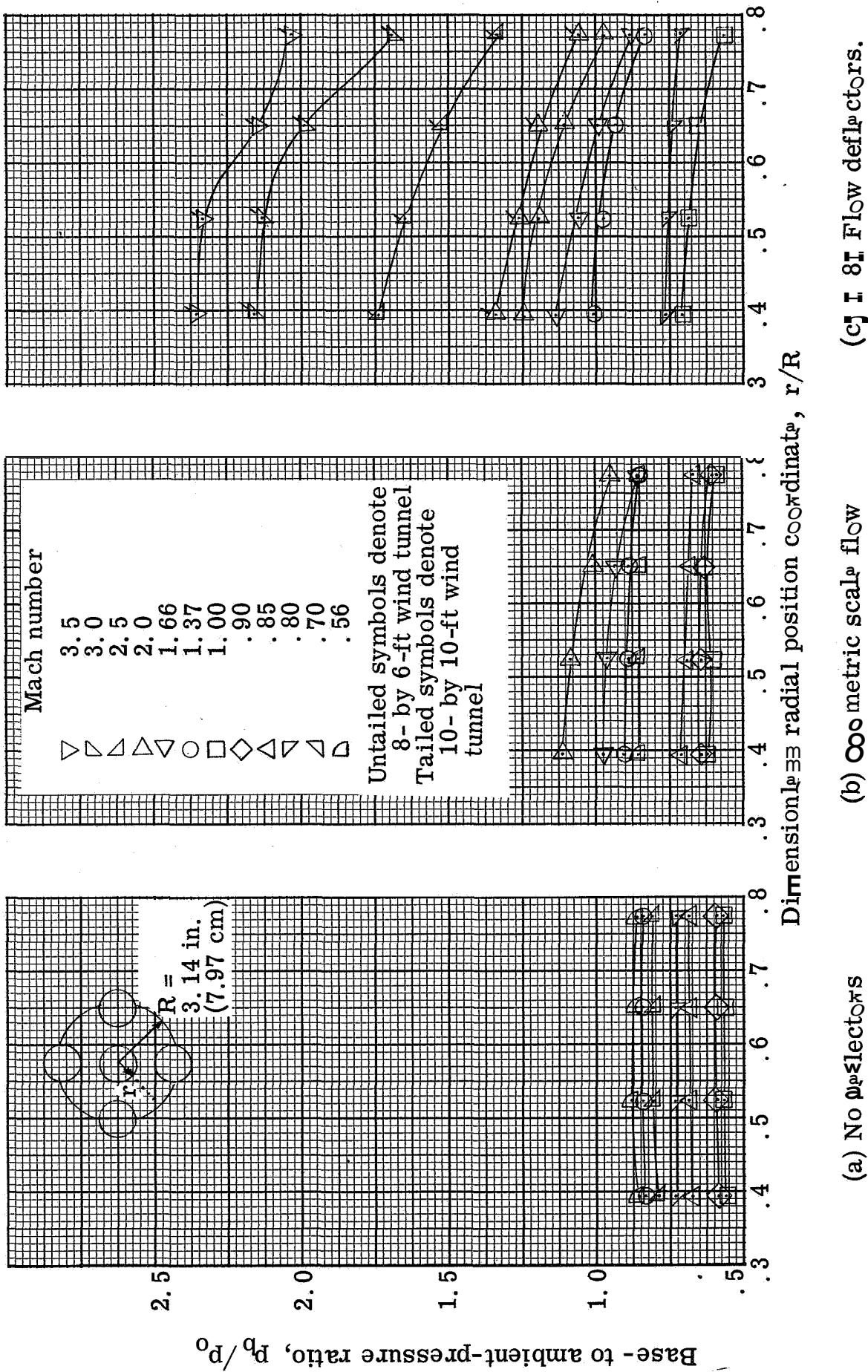


Figure 24. - Effect of flow deflector size on base pressure distribution for 45° roll angle, 0° angle of attack, and 0° gimbal angle.

"The aeronautical and space activities of the United States shall be conducted so as to contribute . . . to the expansion of human knowledge of phenomena in the atmosphere and space. The Administration shall provide for the widest practicable and appropriate dissemination of information concerning its activities and the results thereof."

—NATIONAL AERONAUTICS AND SPACE ACT OF 1958

NASA SCIENTIFIC AND TECHNICAL PUBLICATIONS

TECHNICAL REPORTS: Scientific and technical information considered important, complete, and a lasting contribution to existing knowledge.

TECHNICAL NOTES: Information less broad in scope but nevertheless of importance as a contribution to existing knowledge.

TECHNICAL MEMORANDUMS: Information receiving limited distribution because of preliminary data, security classification, or other reasons.

CONTRACTOR REPORTS: Scientific and technical information generated under a NASA contract or grant and considered an important contribution to existing knowledge.

TECHNICAL TRANSLATIONS: Information published in a foreign language considered to merit NASA distribution in English.

SPECIAL PUBLICATIONS: Information derived from or of value to NASA activities. Publications include conference proceedings, monographs, data compilations, handbooks, sourcebooks, and special bibliographies.

TECHNOLOGY UTILIZATION PUBLICATIONS: Information on technology used by NASA that may be of particular interest in commercial and other non-aerospace applications. Publications include Tech Briefs, Technology Utilization Reports and Notes, and Technology Surveys.

Details on the availability of these publications may be obtained from:

SCIENTIFIC AND TECHNICAL INFORMATION DIVISION
NATIONAL AERONAUTICS AND SPACE ADMINISTRATION

Washington, D.C. 20546